1992ApJ...394..158V

THE ASTROPHYSICAL JOURNAL, 394:158–173, 1992 July 20

A MULTIWAVELENGTH STUDY OF THE SUPERNOVA REMNANT N49 IN THE LARGE MAGELLANIC CLOUD

OLAF VANCURA[1] AND WILLIAM P. BLAIR[1,2]
Center for Astrophysical Sciences, Department of Physics and Astronomy, The Johns Hopkins University,
34th and Charles Streets, Baltimore, MD 21218
KNOX S. LONG[1,2,3]
Space Telescope Science Institute, 3700 San Martin Drive, Baltimore, MD 21218
AND
JOHN C. RAYMOND[1]
Harvard-Smithsonian Center for Astrophysics, 60 Garden Street, Cambridge, MA 02138
Received 1991 November 25; accepted 1992 January 30

ABSTRACT

Using the 2.5 m du Pont telescope at Las Campanas, the *International Ultraviolet Explorer* satellite, and archival high-resolution imager X-ray data from the *Einstein Observatory*, we present a detailed imaging and spectroscopic study of the supernova remnant (SNR) N49 in the Large Magellanic Cloud. Although the X-ray and optical morphology of N49 are similar in the sense that the SNR is brightest in the southeast, the SNR is more circular and extended in the X-ray map, and individual features in the optical and X-ray images do not in general correspond with one another. The asymmetry of the optical image and the relatively high X-ray and optical luminosity of this remnant both arise from its interaction with an extended dense cloud to the southeast seen in CO emission. The optical spectra reveal clear evidence of reddening variations on spatial scales as small as $\sim 2''$ over the face of the SNR. Ultraviolet line emission is associated primarily with the bright optical filaments, and we measure the total luminosity of N49 in several optical and UV lines. A combined analysis of *IUE* and optical spectra indicates a range of radiative shock velocities. The bulk of the observed emission emanates from shocks with velocities ≤ 140 km s^{-1}, although echelle data indicate that faint shocks ≥ 200 km s^{-1} must be present. Upon modeling the spectrum, we find that a power-law velocity distribution corresponding to 40 km s$^{-1} \leq V_s \leq 270$ km s^{-1} provides a good match, with the bulk of the emission arising from the slower shocks. Preshock densities of 20–940 cm^{-3} and postshock nonthermal pressure support are required to account for both the total optical and UV luminosities and the densities inferred from the [S II] doublet. We derive improved elemental abundances for N49. We conclude by discussing implications for the interstellar medium surrounding N49. We develop a model invoking a Sedov solution in which the main blast wave also encounters large clouds. For this model, we demonstrate that the energetics of N49's evolution as a whole and blast wave/cloud interactions on a smaller scale are self-consistent.

Subject headings: ISM: individual (N49) — ISM: structure — Magellanic Clouds — shock waves — supernova remnants — ultraviolet: spectra

1. INTRODUCTION

To date, 32 supernova remnants (SNRs) have been identified in the Large Magellanic Cloud (LMC) through a combination of radio, optical, and X-ray techniques (Long, Helfand, & Grabelsky 1981; Mathewson et al. 1983, 1985). In more distant and more reddened galaxies, selection effects necessarily limit the SNRs that will be discovered to the most luminous objects. N49 has the highest optical surface brightness of any SNR in the LMC (Dopita 1979), and it is the third brightest X-ray SNR (Long et al. 1981). Therefore, N49 is likely to resemble SNRs most readily detectable in extragalactic surveys. A more complete understanding of this remnant, and its relationship to lower surface brightness and/or fainter SNRs, is important.

N49 was first identified as a SNR by Mathewson, Healey, & Westerlund (1963). The first detailed optical study of N49 was by Osterbrock & Dufour (1973), who compared the emission-line spectrum to the pioneering radiative shock wave models of Cox (1972). At an assumed distance to the LMC of 50 kpc (Eastman & Kirshner 1989), N49's angular diameter of $\sim 1'$ corresponds to a physical diameter of ~ 16 pc. Age estimates of $\sim 10{,}000$ yr are typical (Long et al. 1981; Shull 1983). Optical and X-ray studies show no evidence of progenitor material (Osterbrock & Dufour 1973; Clark et al. 1982). Except for its surface brightness and its positional association with a γ-ray burst source (Cline et al. 1982), N49 appears typical of other middle-aged SNRs in the LMC.

Danziger & Leibowitz (1985) and also Russell & Dopita (1990) have carried out spectroscopic studies of SNRs in the LMC and have found elemental abundances for several remnants. Abundances in N49 differ little from the rest of the LMC. Dennefeld (1986) observed N49 in the optical and near-infrared (IR), and reports reddening in the range $0.44 < E(B-V) < 0.58$. Graham et al. (1987), using *IRAS* observations, suggest that a substantial portion of the far-infrared emission from N49 can be explained by collisionally heated dust.

---

[1] Guest Observer, *International Ultraviolet Explorer*, which is operated by NASA, the Science Research Council of the UK, and the European Space Agency.

[2] Visiting Astronomer, Las Campanas Observatory, which is operated by the Carnegie Institution of Washington.

[3] Visiting Adjunct Associate, Mount Wilson and Las Campanas Observatories.

Benvenuti, Dopita, & D'Odorico (1980) have presented the only previous ultraviolet spectrum of N49, using the *International Ultraviolet Explorer* (*IUE*) satellite. Only a short-wavelength (SWP) spectrum was taken. They report hydrogen two-photon continuum radiation in addition to numerous emission lines. Shull et al. (1985) have proposed a model for the evolution of N49 in which the progenitor star has modified the structure of the ISM around N49. The model invokes a multiphase medium including a density-enhanced shell in an effort to explain the different types of emission and their interrelation.

We have obtained a large body of new data, including optical interference filter CCD images, long-slit CCD spectra, echelle spectra, and pairs of SWP and LWP *IUE* exposures at five locations in N49, in an attempt to construct a more coherent picture of this SNR. By combining these new data with previous archival X-ray observations, we hope to achieve a better global understanding of N49. We present the optical, UV, and X-ray observations of N49 in § 2. We analyze the observations and discuss their implications in § 3. We attempt to explain the reasons for N49's striking brightness and overall morphology in § 4. Finally, we briefly summarize our results in § 5.

2. OBSERVATIONS AND REDUCTIONS

2.1. *Imaging*

We obtained images of N49 using a TI 800 × 800 CCD with a focal reducer on the 2.5 m du Pont telescope at Las Campanas Observatory (LCO) on 1987 November 11–12. The CHUEI focal reducer is similar to the PFUEI described previously by Gunn & Westphal (1981). On the 2.5 m telescope, the CHUEI yielded a scale of 0.″41 pixel^{-1} on the CCD and a 5.′5 field of view. Conditions were photometric on both nights, and images were obtained in Hα, [O I] λ6300, [O III] λ5007, [S II] λλ6717, 6731, [S III] λ9069, and a continuum band near 6100 Å. Table 1 lists the interference filters and exposure times. Each night the standard stars LTT 2415 and LTT 377 from Stone & Baldwin (1983) were observed through the filters.

The images were all reduced at Johns Hopkins using IRAF.[4] The images were bias-subtracted, and divided by normalized dome flat fields to take out pixel-to-pixel variations in the CCD. Seeing in the original images ranged from 1.″18 FWHM in Hα to 1.″39 FWHM in [O III]. To facilitate comparison, for each of the images we have smoothed to the resolution of the [O III] image and sky-subtracted. Finally, we have aligned all the images. In Figure 1 (Plates 2–4) we present the reduced images of N49. Panels *a*, *c*, *e*, and *g* show N49 in the light of Hα [O I], [O III], and [S II], respectively, with contrast adjusted to show the bright filaments. In panels *b*, *d*, *f*, and *h*, we show "stretched" versions of the images to emphasize the ubiquity and extent of faint emission. Figure 1*i* is N49 in the light of [S III], and Figure 1*j* is the image resulting from the 6100 Å continuum filter.

At optical wavelengths, N49 appears as a bright, semicircular, filamentary crescent, opening with very faint emission to the northwest. There is a particularly bright ridge of emission in the east and southeast. At lower surface brightness levels, optical emission is more extended along the periphery and is also seen to more nearly cover the face of N49. The "stretched" Hα map shows evidence of a faint H II region in the northwest portion of the image, in addition to a faint Hα enhancement in the western part of N49 itself. Thus, at faint light levels, N49 exhibits a relatively circular appearance. This is consistent with the X-ray image (see below).

To obtain luminosities in these optical lines, we have scaled and subtracted the continuum image from each of the emission-line images to remove stellar contamination. This procedure is not exact because there is clearly some emission associated with the continuum image, and some stellar residuals remain. However, the effect is less than 15% for [S III] and less than 5% in all other cases. The total counts corresponding to SNR emission were converted to absolute flux units by comparison with the standard stars observed through the same filters. We have also estimated the SNR flux in the 6100 Å continuum image; in this case, stars were excluded individually from the total counts before fluxing. Observed and intrinsic (i.e., reddening-corrected) total luminosities of N49 are presented in Table 2, assuming a distance to N49 of 50 kpc and $E(B-V) = 0.37$ as found in § 2.2. The fluxes obtained in this way are only approximate. Comparing raw fluxes at regions observed with the long-slit spectroscopy of § 2.2, we estimate the uncertainty to be $\leq 50\%$ for all images. Variations in extinction could cause additional uncertainty in these luminosities. We have calculated the effects of various spatial reddening distributions on optical line strengths and find the effect to be $\leq 10\%$ for conditions typical of N49 (see § 2.2).

Ratio maps were obtained by dividing the various aligned emission-line images pixel by pixel. Pixels corresponding to values near zero in the denominator image were set to zero in the resultant image as well, to avoid division by small numbers. Figures 2*a*–2*d* (Plate 5) present ratio maps of N49 in [O I]:Hα, [O III]:Hα, [S II]:Hα, and [O III]:[O I]. High

TABLE 1

INTERFERENCE FILTER/CCD IMAGING OF N49

Filter	Central Wavelength (Å)	FWHM (Å)	Integration Time (s)
Hα	6565	30	1000
[O I]	6300	50	1000
[O III]	5027	53	1000
[S II]	6737	57	1000
[S III]	9080	50	1000
Continuum	6100	130	1000

TABLE 2

OBSERVED FLUXES AND INTRINSIC TOTAL LUMINOSITIES[a] OF N49

Filter	$F(\lambda)$ (ergs s^{-1} cm^{-2})	$L(\lambda)$ (ergs s^{-1})
Hα	4.2×10^{-11}	2.9×10^{37}
[O I]	1.5×10^{-11}	1.1×10^{37}
[O III]	1.4×10^{-11}	1.4×10^{37}
[S II]	3.9×10^{-11}	2.6×10^{37}
[S III]	3.0×10^{-12}	1.5×10^{36}
Continuum[b]	1.9×10^{-12}	1.5×10^{36}

[a] Assumes $E(B-V) = 0.37$ and a distance of 50 kpc to N49.
[b] Over 130 Å bandpass centered at 6100 Å.

---

[4] IRAF is distributed by the National Optical Astronomy Observatories, which is operated by the Association of Universities for Research in Astronomy (AURA), Inc., under cooperative agreement with the National Science Foundation.

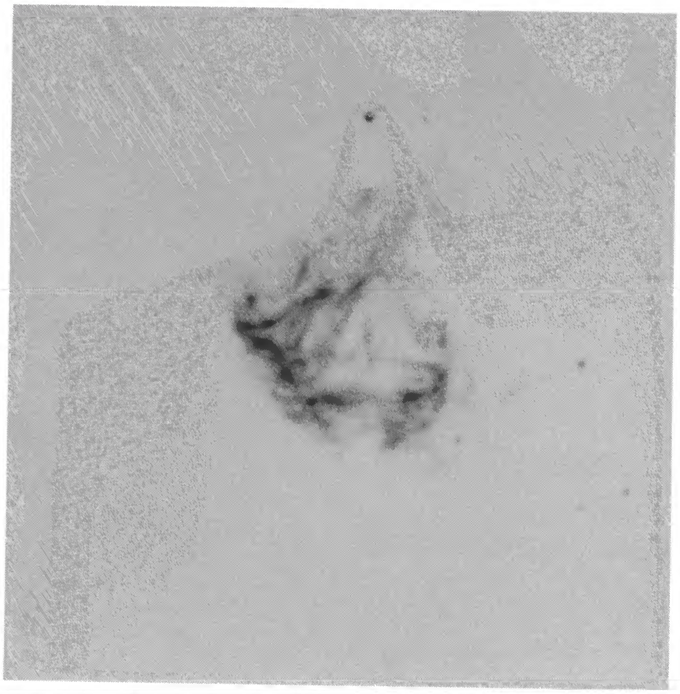

FIG. 1*a*

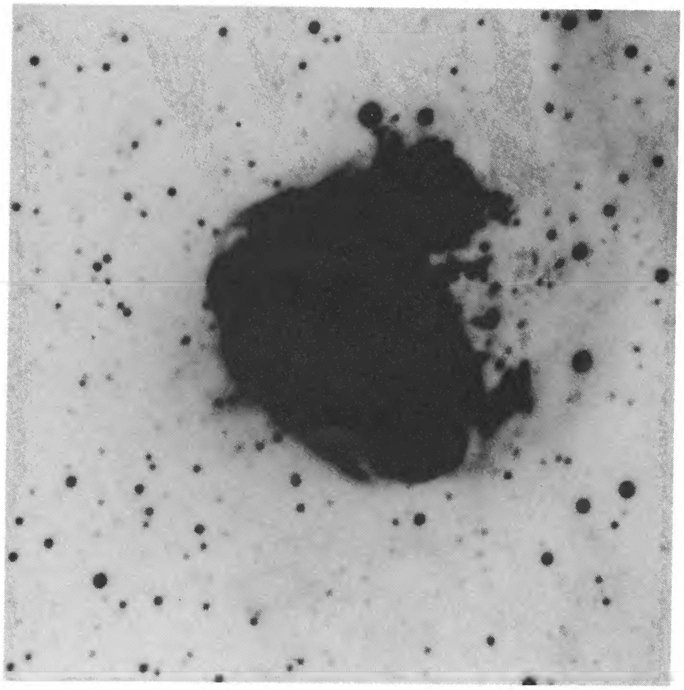

FIG. 1*b*

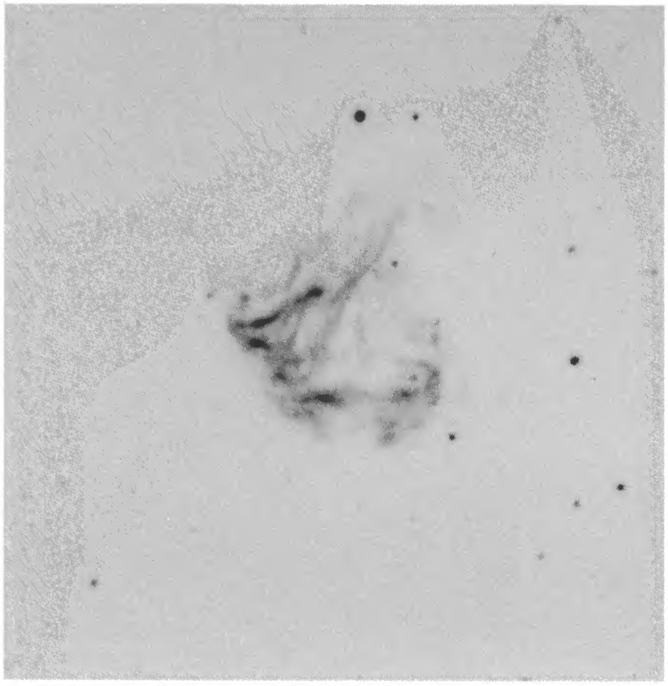

FIG. 1*c*

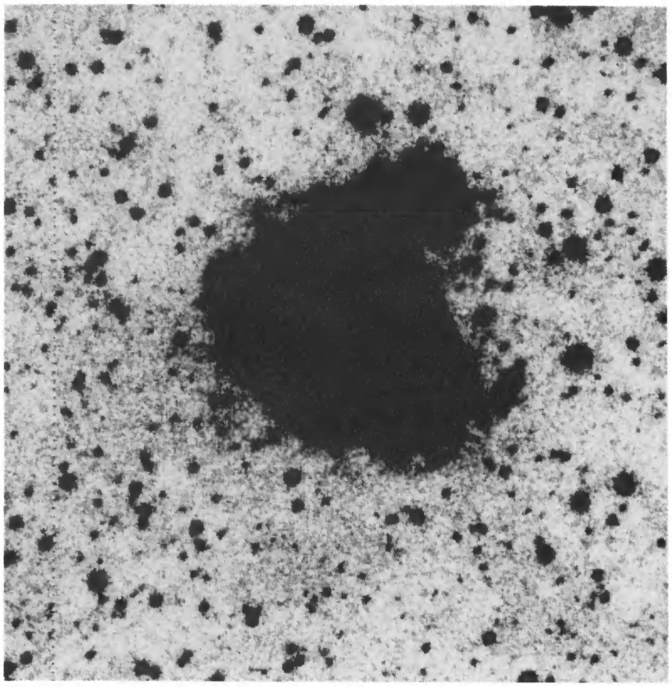

FIG. 1*d*

FIG. 1.—N49 images in the light of (*a*, *b*), Hα, (*c*, *d*), [O I], (*e*, *f*) [O III], (*g*, *h*) [S II], (*i*) [S III], and (*j*) 6100 Å continuum. Each emission-line image (except [S III]) is presented twice to show the bright filaments and extent of faint emission. (*k*) Overlaid on the [O III] image is a contour map of the reprocessed *Einstein* X-ray image, smoothed to a resolution of 4″. (*l*) Marked on the [O III] image are the locations for the long slits and *IUE* apertures. Also delineated are several locations where spectra were extracted that are referred to in the text.

VANCURA, BLAIR, LONG, & RAYMOND (see 394, 159)

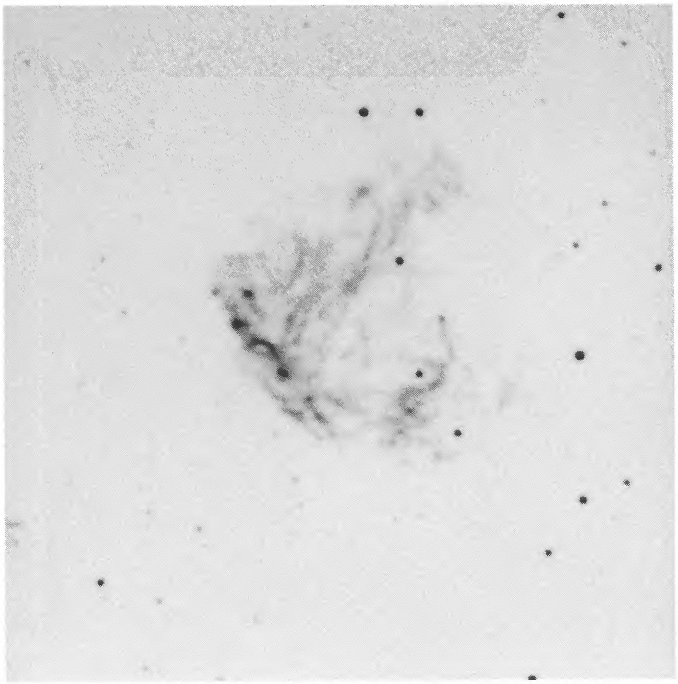

FIG. 1*e*

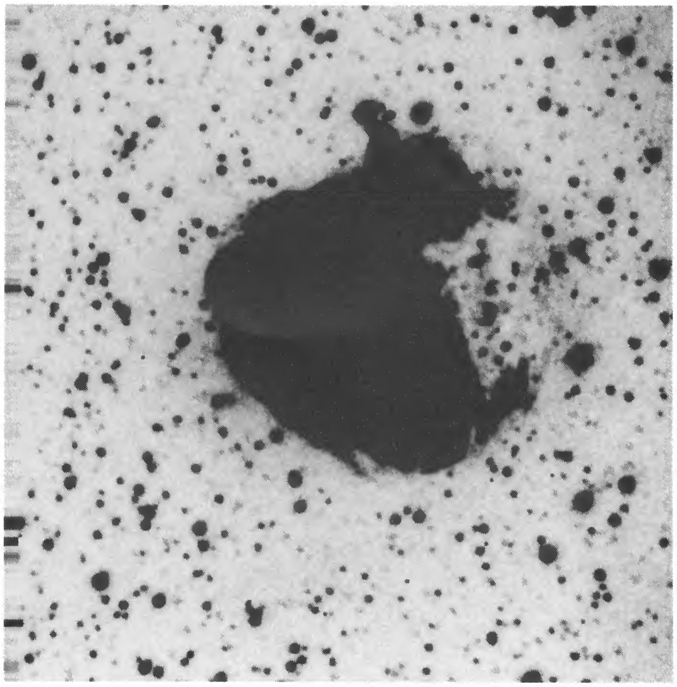

FIG. 1*f*

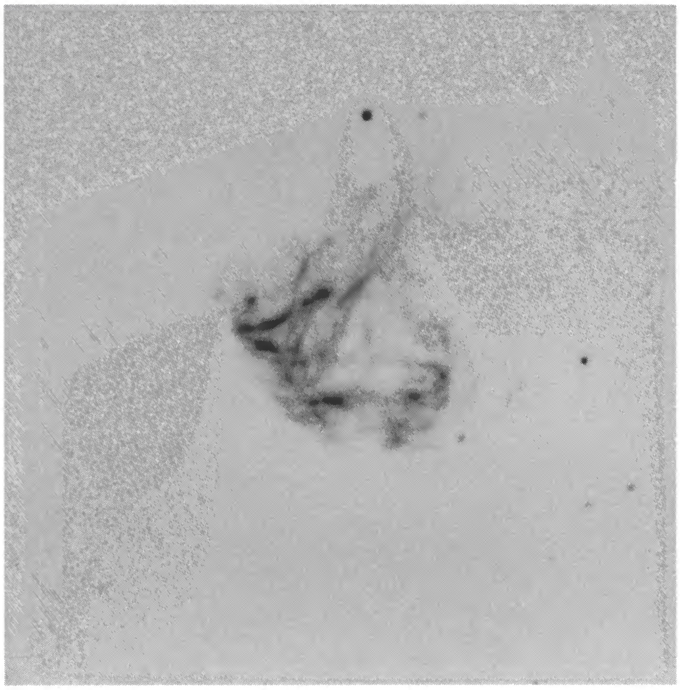

FIG. 1*g*

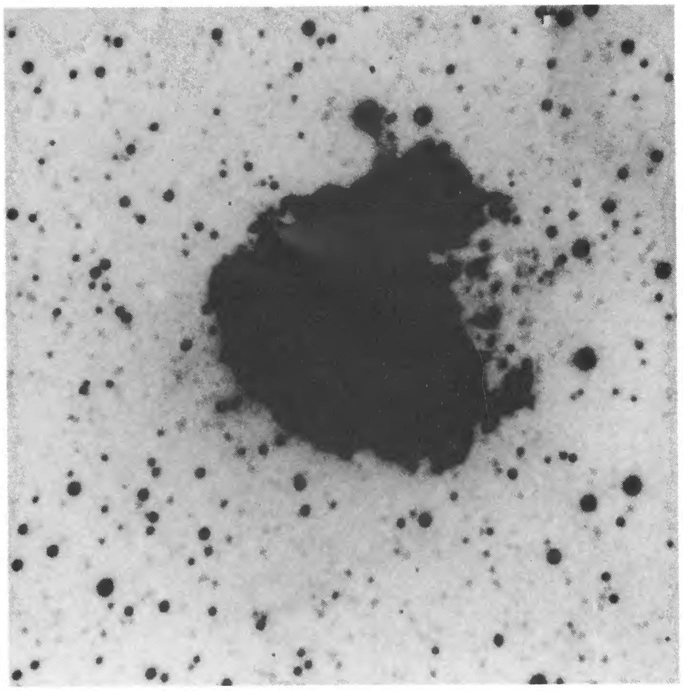

FIG. 1*h*

VANCURA, BLAIR, LONG, & RAYMOND (see 394, 159)

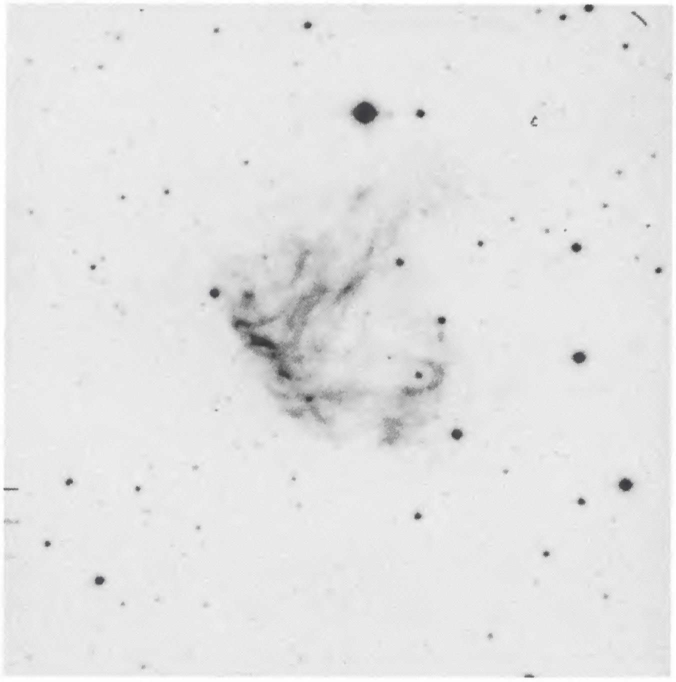

FIG. 1*i*

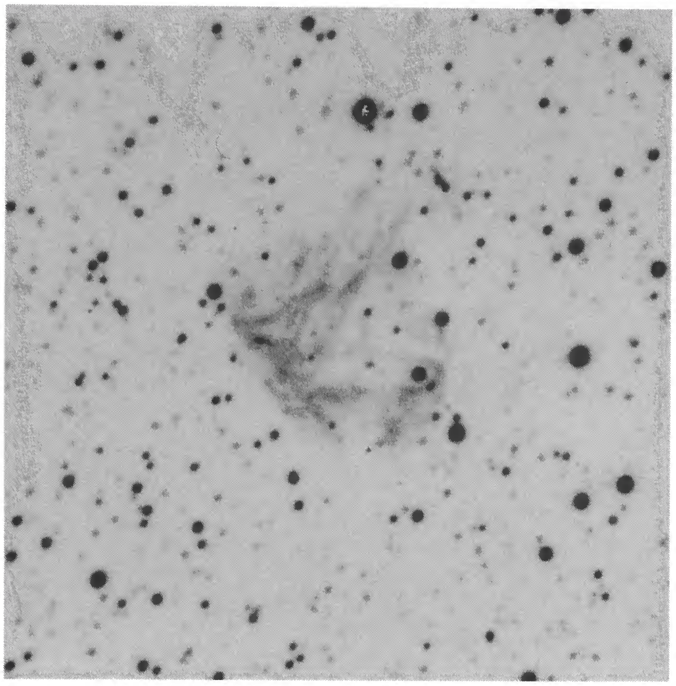

FIG. 1*j*

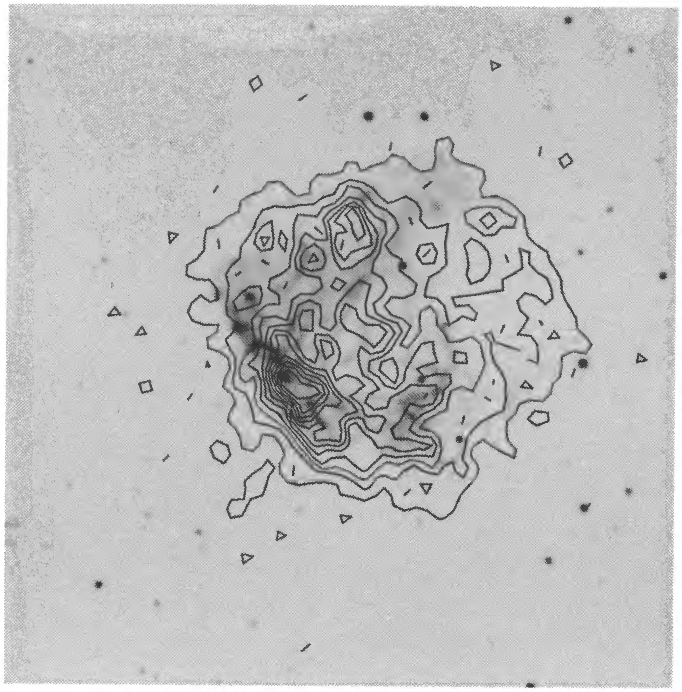

FIG. 1*k*

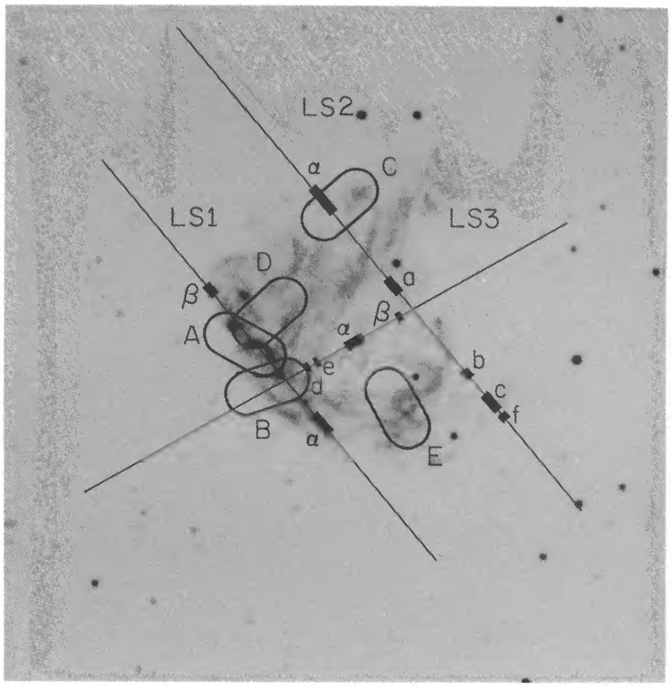

FIG. 1*l*

VANCURA, BLAIR, LONG, & RAYMOND (see 394, 159)

1992ApJ...394..158V

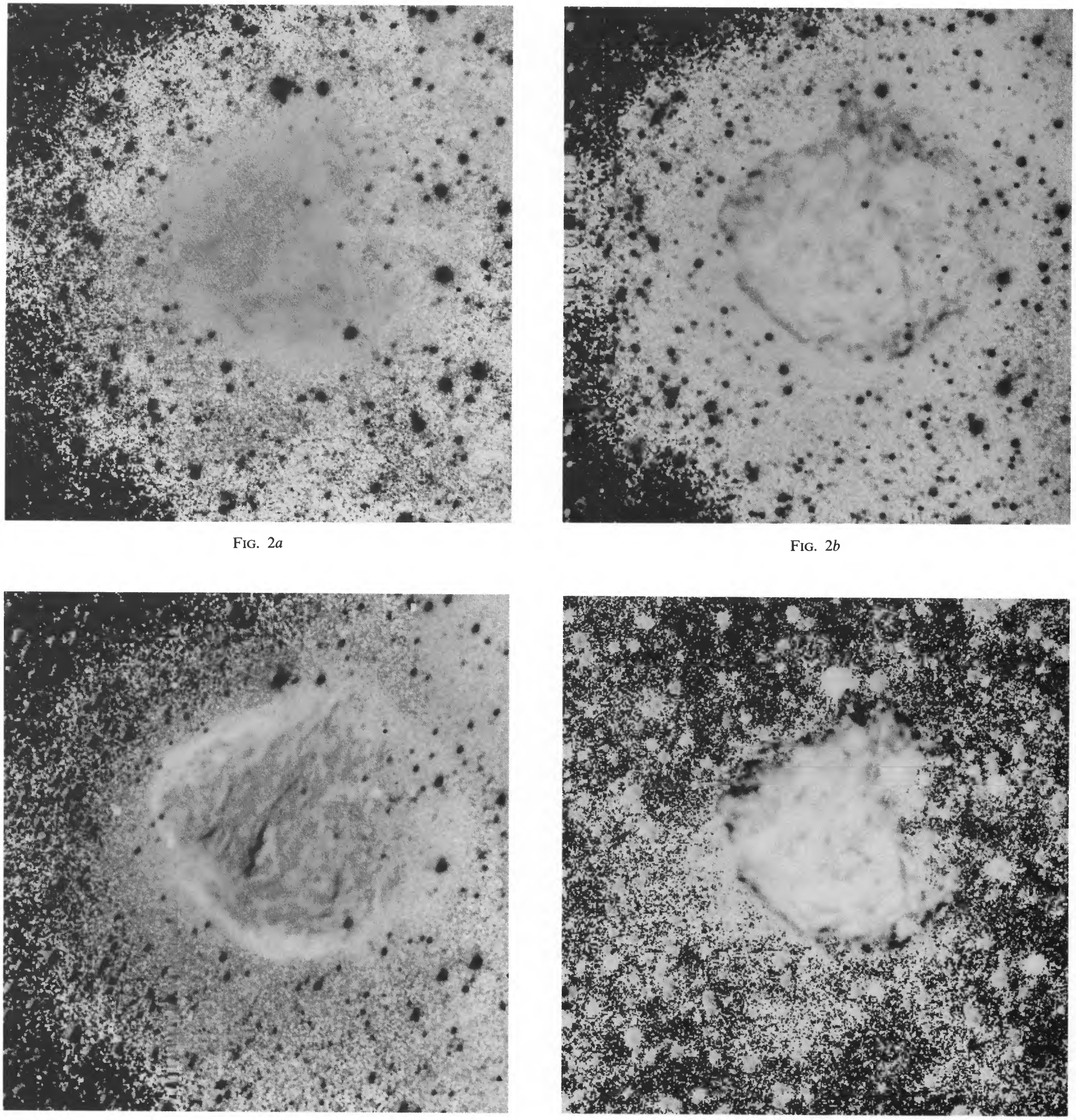

FIG. 2*a*

FIG. 2*b*

FIG. 2*c*

FIG. 2*d*

FIG. 2.—N49 emission-line ratio maps. The panels are (*a*) [O I]:Hα, (*b*) [O III]:Hα, (*c*) [S II]:Hα, (*d*) [O III]:[O I]. Note in particular the bright ringlike zone of enhancement on panels *b* and *d*. Owing to noise fluctuations, the ring is more difficult to discern in panel *d*, but close inspection indicates that features comprising the ring are correlated well between the two images.

VANCURA, BLAIR, LONG, & RAYMOND (see 394, 159)

1992ApJ...394..158V

values of the ratio are dark; low values are light in these maps. The morphology of the emission from N49 in Hα, [O I], and the interior of the [S II] is very similar, as evidenced by the fact that the ratio maps show little structure. This is expected, since the conventional understanding of these emissions suggests that [O I], Hα, and [S II] arise in the coolest (10^4 K) regions of the recombination flow. On the other hand, the distribution of [O III] emission differs from that of the low-ionization lines, as revealed in the [O III]:[O I] and [O III]:Hα maps. Specifically, there is a "ring" or "zone" of high [O III]:Hα (or [O III]:[O I]) that can be traced around much of the periphery of the remnant. The fact that this ring is visible in both the [O III]:[O I] and [O III]:Hα maps implies that the existence of this zone is an ionization rather than an abundance effect. Close inspection reveals that the peak of the [O III]:[O I] map in general does *not* coincide with the brightest [O III] emission. Rather, it lies some 0.1–0.8 pc in front of the bright [O III]. The [O III]:Hα map also shows a partial ring of enhanced Hα immediately outside the ring of high [O III]:Hα.

We have requested and obtained reprocessed high-resolution imager (HRI) *Einstein* data on N49 from the *Einstein* on-line data archive in order to compare the X-ray emission with the optical emission. These data have been aligned with the optical data and smoothed with a Gaussian filter to a resolution of 4″. The X-ray contour map is shown overlaid on the [O III] map in Figure 1*k*. There are some similarities. Both the X-ray and the optical images are brightest in the southeast; neither the X-ray nor the optical emission shows a well-developed shell. On the other hand, individual features, i.e., knots, in the X-ray and optical maps do not exhibit a one-to-one correspondence. The X-ray image is more circular and indicates a larger diameter. The soft (0.1–4.5 keV) X-ray luminosity of 1.9×10^{37} ergs s^{-1} (Long et al. 1981) is comparable to the luminosities of individual optical emission lines as shown in Table 2.

Presuming that the leading X-rays track the main blast wave, the bright optical shocks have formed where this blast wave encountered density enhancements in the ISM. Both the optical and X-ray maps suggest large-scale density gradients in the vicinity of N49. Recently, Hughes, Bronfman, & Nyman (1989) have discovered a large CO cloud to the southeast of N49. The SNR is clearly interacting with this cloud over most of its southeast quadrant. The absence of optical emission (save for the faint Hα in the west), coupled with the fainter, more circular X-ray appearance, is consistent with a region in which the main blast wave has encountered a low-density intercloud medium (ICM) devoid of clouds. The overall X-ray contours show a pronounced increase of brightness from northwest to southeast. This is consistent with the higher pressure expected where the blast wave encounters a large dense cloud, but it is also possible that a higher density ICM in this region leads to a lower temperature, higher density X-ray–emitting gas in pressure equilibrium with the rest of the remnant.

2.2. *Long-Slit Spectroscopy*

We have obtained long-slit CCD spectra at the three positions indicated in Figure 1*l*. These spectra were taken in 1989 February with the modular spectrograph on the 2.5 m du Pont telescope at LCO using TI 800 × 800 CCD. An observing log is presented in Table 3. Three different setups were used. The blue spectra were obtained with a 600 line mm^{-1} 5000 Å blaze grating and 2″ slit width yielding coverage from 4750 to 7150 Å. The red and IR data were both obtained with a 600 line mm^{-1} 7500 Å blaze grating and 2″ slit width. The red coverage was from 6250 to 8650 Å, while the IR wavelength range was from 8100 to 10500 Å. All spectra had ~8 Å resolution. Blue and red spectra were taken for positions LS1, LS2, and LS3, while IR spectra were obtained for position LS1 only. The spatial scale provided by the "fast" camera (focal length 85 mm) was 0″.85 $pixel^{-1}$.

We reduced these spectra using IRAF. Each two-dimensional spectrum was background-subtracted to correct for scattered light, flat-fielded, transformed to remove spectrograph distortions, and wavelength-calibrated. Flux calibration was applied using observations of spectrophotometric standard stars each night from the list of Stone & Baldwin (1983). Comparison of the reduced spectra of the standard stars LTT 2415, LTT 3864, and LTT 6248 indicates an absolute accuracy of 30%, 10%, and 20% for the blue, red, and IR ($\lambda \leq 10000$ Å) spectra, respectively. The uncertainties in relative calibration between the long- and short-wavelength ends of the blue, red and IR are 15%, 5%, and 10%, respectively.

One-dimensional spectra were extracted from various portions along each slit. Regions for sky subtraction were chosen from adjacent regions along the slit not showing any SNR emission. Overall, there is little variation in the optical characteristics of different bright optical filaments. Figures 3 and 4 show samples of one-dimensional spectra, with regions for extraction indicated on Figure 1*l*. Figures 3*a*–3*c* are the full wavelength coverage of a region co-observed as *IUE* position A (§ 2.4). Figure 4*a* shows a region extracted near the center of LS2, where the optical emission is relatively faint. Figure 4*b* shows an extraction from LS2 in the southwest part of N49. The observed Hα:Hβ ratio indicates that there is effectively no

TABLE 3

SPECTROPHOTOMETRIC OBSERVATIONS OF N49

Slit Position[a]	Date (UT)	Wavelength Configuration[b]	Integration Time (s)	Position Angle	Condition
LS1...........	1989 Feb 11	Blue	300	40°	Hazy
LS1...........	1989 Feb 12	IR	1500	40	Hazy
LS1...........	1989 Feb 18	Red	100	40	Clear
LS2...........	1989 Feb 11	Blue	300	40	Hazy
LS2...........	1989 Feb 18	Red	300	40	Clear
LS3...........	1989 Feb 11	Blue	300	120	Hazy
LS3...........	1989 Feb 18	Red	600	120	Clear

[a] See Fig. 1*l* for slit positions.

[b] See text for exact wavelength ranges.

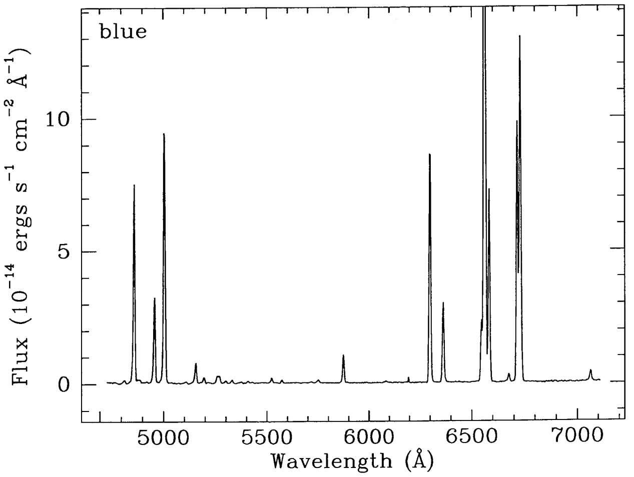

FIG. 3*a*

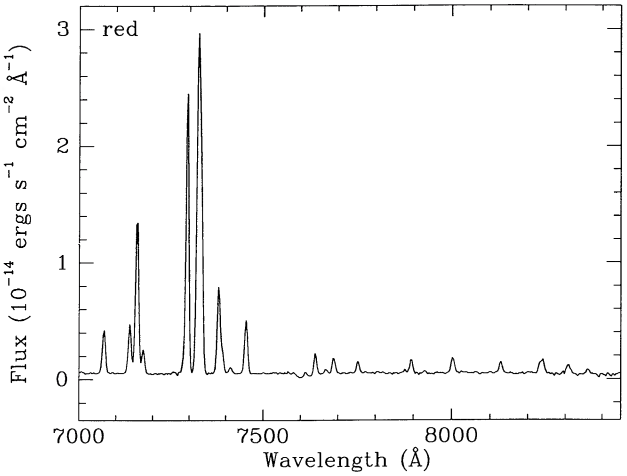

FIG. 3*b*

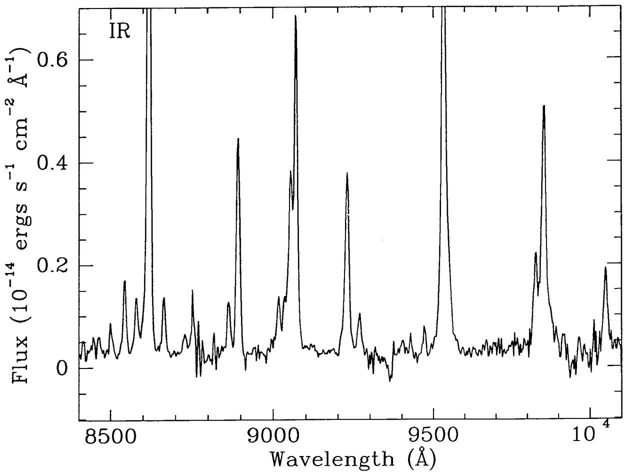

FIG. 3*c*

FIG. 3.—Portion of the long-slit spectrum corresponding to *IUE* position A. Panels *a*, *b*, and *c* are the blue, red, and IR bandpasses, respectively.

reddening along this line of sight (see below). Figure 4*c* corresponds to the region of relatively enhanced [O III]:[O I] in the southwest from slit position LS2. Figures 4*d* and 4*e* exemplify the variation in reddening seen to N49. They are taken from regions in the east whose centers are ~3″ apart, yet the reddening indicated by the Balmer lines to the position in Figure 4*d* is $E(B-V) = 0.10$, while that to the position in Figure 4*e* is 0.50. Figure 4*e* also shows enhanced [S II] emission, visible as a dark wisp near the center of emission in the [S II]:Hα ratio map (Fig. 2*c*). We note that in general there is little variation in relative line strengths across the face of N49; in this regard Figures 3, 4*a*, and 4*d* are representative of typical spectra.

Figure 4*f* shows a region whose spectrum is dominated by the hydrogen Balmer lines. This extraction is in the southwest, taken from a region adjacent to Figure 4*c*. The observed surface brightness in Hα is 5.42×10^{-16} ergs cm^{-2} s^{-1} $arcsec^{-2}$. This may be a nonradiative shock (see Chevalier, Kirshner, & Raymond 1980; Smith et al. 1991). If this identification is correct, it would be the first time such emission has been seen in N49 and would indicate that the primary shock is encountering partly neutral preshock gas. However, Chu & Kennicutt (1988) report an H II region to the west of N49. Our long-slit data confirm this, and spectra of the H II region taken 1′ west of any SNR optical emission along LS2 yield an observed surface brightness of 1.0×10^{-16} and 4.4×10^{-16} ergs cm^{-2} s^{-1} $arcsec^{-2}$ for [O III] and Hα, respectively. This Hα surface brightness is close to that of the region extracted for Figure 4*f*, but the Figure 4*f* spectrum comes from a spatially narrow region directly associated with the SNR. Unfortunately, the faintness of the emission in Figure 4*f* is such that it precludes measurement of any broad component that would confirm the nonradiative shock ascription. Furthermore, with 8 Å resolution, only shocks with velocity exceeding 500 km s^{-1} would have a detectable broad component. It is conceivable that shock precursor emission could also be responsible for the spectrum in Figure 4*f*.

Line intensities and identifications of sample spectra are tabulated in Tables 4A and 4B. The scale is such that Hβ = 100, with the measured and corrected Hβ fluxes for each spectrum being given as well. We have dereddened the spectra assuming the standard Whitford (1958) reddening law, with the reddening function of Savage & Mathis (1979), and an intrinsic Hα:Hβ ratio of 3.0 (cf. Hummer & Storey 1987) to determine $E(B-V)$, also given in Table 4. We defer to § 3 a discussion of the validity of this intrinsic ratio.

Previously, some investigators have found essentially no reddening to N49, with others finding the extinction to be quite substantial (Osterbrock & Dufour 1973; Dennefeld 1986). We have determined values for $E(B-V)$ at many different positions in N49 to investigate variations in the extinction along different lines of sight. For the entire length of the three positions LS1, LS2, and LS3, we find values for $E(B-V)$ of 0.40, 0.34, and 0.39, respectively. Summing all the spectra yields an average $E(B-V) = 0.37$. Typical values of $E(B-V)$ on smaller spatial scales range from 0.3 to 0.5 mag. Reddening varies by significant amounts on spatial scales as small as 2″. Several locations show particularly high reddening—for example, Figure 4*e*, apertures LS1-α with $E(B-V) = 0.61 \pm 0.07$ (1 σ), LS1-β with $E(B-V) = 0.93 \pm 0.30$, LS2-α with $E(B-V) = 0.51 \pm 0.16$, and LS3-α with $E(B-V) = 0.53 \pm 0.05$. We also see locations with anomalously low reddening, in particular Figures 4*b* and 4*d*, in addition to location LS3-β as indicated on Figure 1*c*, with

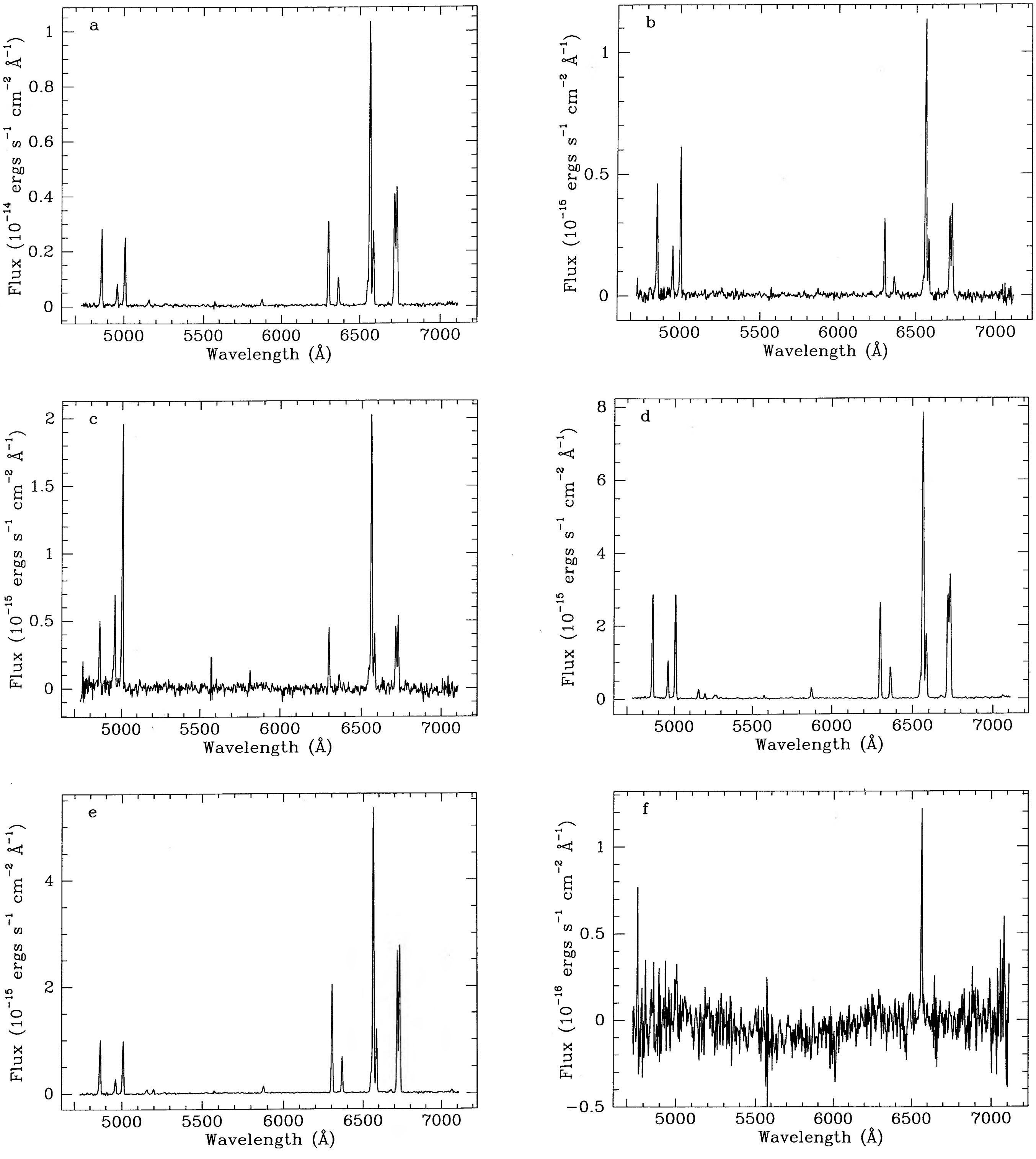

FIG. 4.—One-dimensional spectra for various selected N49 positions. The extracted apertures are shown in Fig. 1*l*. See text for description.

$E(B-V) = 0.0 \pm 0.10$. The spectra associated with high [O III]:[O I] have $E(B-V)$ between 0.25 and 0.56, with an average of 0.37. Thus, as a set they show nothing irregular compared with other locations. As the extinction in our Galaxy in the direction of the LMC is typically $E(B-V) = 0.07$ (cf. Fitzpatrick 1985), it appears that the bulk of the extinction must be intrinsic to the LMC (and may be local to N49).

2.3. *Echelle Observations*

We obtained echelle spectra of N49 at LCO on 1988 April 26 using the 2D-Frutti detector and a high-resolution grating.

TABLE 4A

OBSERVED AND DEREDDENED OPTICAL FLUXES FOR *IUE* POSITION A

Line	$F(\lambda)$	$I(\lambda)$	Line	$F(\lambda)$	$I(\lambda)$
Hβ λ4861[a]	100	100	[Ni II] λ7413	0.9	0.6
[O III] λ4959	43.0	41.7	[Fe II] λ7453	6.7	4.1
[O III] λ5007	134	128	[Fe II] λ7638	2.6	1.5
[Fe II] λ5159	11	10	λ7666	0.9	0.5
[N I] λ5200	3.4	3.0	[Fe II] λ7687	2.5	1.5
[Fe II] λ5262	3.9	3.5	[Ar III] λ7752	1.9	1.1
[Fe III] λ 5270	3.9	3.5	[Cr II] λ8002	2.2	1.3
[Fe XIV] λ5303	2.1	1.8	[Cr II] λ8127	1.6	0.9
[Fe II] λ5332	2.2	1.9	[Cr II] λ8231	3.1	1.7
[Fe II] λ5527	2.5	2.1	[Cr II] λ8310	1.9	1.0
[O I] λ5576	1.6	1.3	[Cr II] λ8359	0.7	0.4
[N II] λ5755	2	1.6	Ca II + Pa15 λ8545	1.5	0.8
He I λ5876	14.1	10.9	[Cl II] λ8580	1.1	0.6
[Fe VII] λ6085	1.3	1.0	[Fe II] λ8617	25.5	13.5
λ6198	1.3	0.9	Ca II + Pa13 λ8665	1.8	1.0
[O I] λ6300	125	89.6	[C I] λ8730	0.8	0.4
[O I] λ6363	42.3	30.0	Pa12 λ8750	1.1	0.6
[N II] λ6548	28.7	19.8	Pa11 λ8863	1.7	0.9
Hα λ6563	436	300	[Fe II] λ8892	8.0	4.1
[N II] λ6584	101	69.3	Pa10 λ9015	2.1	1.1
He I λ6678	4.1	2.8	[Fe II] λ9037	2.6	1.3
[S II] λ6717	133	89.8	[Fe II] λ9052	7.5	3.8
[S II] λ6731	179	121	[S III] λ9069	11.2	5.7
He I λ7065	6.2	4.0	[Fe II] λ9227	7.3	3.7
[Ar III] λ7136	6.2	4.0	[Fe II] λ9267	1.5	0.7
[Fe II] λ7155	19.7	12.6	[Fe II] λ9470	0.7	0.3
[Fe II] λ7172	3.4	2.1	[S III] λ9532	23.3	11.4
[Ca II] λ7292	32.7	20.4	[C I] λ9823	4.3	2.1
[O II] + [Ca II] λ7325	67.3	41.8	[C I] λ9850	12.1	5.8
[Ni II] λ7380	11.7	7.2	Pa7 λ10055	3.0	1.4

[a] $F(\mathrm{H}\beta)$ and $I(\mathrm{H}\beta)$ in units of ergs cm^{-2} s^{-1} are 6.82×10^{-13} and 2.14×10^{-12}, respectively. This equals 100 in the units of the table. $E(B-V) = 0.35$.

TABLE 4B

OBSERVED AND DEREDDENED OPTICAL FLUXES FOR SELECTED N49 FILAMENTS

	FIG. 4*a*		FIG. 4*b*		FIG. 4*c*		FIG. 4*d*		FIG. 4*e*	
LINE	$F(\lambda)$	$I(\lambda)$	$F(\lambda)$	$I(\lambda)$	$F(\lambda)$	$I(\lambda)$	$F(\lambda)$	$I(\lambda)$	$F(\lambda)$	$I(\lambda)$
Hβ λ4861	100	100	100	100	100	100	100	100	100	100
[O III] λ4959	27.8	27	46.6	46.5	121	117	32.2	31.9	26.8	25.6
[O III] λ5007	95.7	91.4	142	142	381	363	100	98.8	94.4	88.4
[Fe II] λ5159	8.9	8.1	...	...	...	...	11.8	11.5	10.1	8.9
[N I] λ5200	...	...	...	...	...	...	5.7	5.5	9.8	8.5
[Fe II] λ5262	...	...	...	...	...	...	4.2	4.1	...	...
[Fe III] λ5270	...	...	...	...	...	...	4.2	4.0	...	...
[Fe XIV] λ5303	...	...	...	...	...	...	1.7	1.7	...	...
[O I] λ5576	...	...	...	...	...	...	3	2.8	4.3	3.2
He I λ5876	11.3	8.7	...	...	...	...	10.8	10.1	13.5	9.3
[O I] λ6300	123	88.4	72.4	71.3	84.7	59.2	107	97.8	180	112
[O I] λ6363	42	29.9	22.5	22.2	27.8	19.2	35.6	32.4	59.9	36.8
[N II] λ6548	36.1	24.9	25.8	25.4	39.4	26.4	50.2	45.4	41.2	24.3
Hα λ6563	435	300	305	300	449	300	332	300	511	300
[N II] λ6584	109	75	59.9	58.9	80.1	53.4	72.1	65.1	112	65.5
He I λ6678	2.1	1.5	...	...	...	...	...	...	...	...
[S II] λ6717	179	121	90.5	88.9	101	66.1	128	115	253	145
[S II] λ6731	184	124	105	103	119	77.8	155	139	265	151
Hβ λ4861[a]	24.8	77.1	3.55	3.73	4.31	14.8	26.7	36.4	9.87	50.2
$E(B-V)$	0.35		0.02		0.38		0.10		0.50	

[a] $F(\mathrm{H}\beta)$, $I(\mathrm{H}\beta)$ in units of 10^{-15} ergs cm^{-2} s^{-1}. This equals 100 in the units of the table.

1992ApJ...394..158V

With good blue sensitivity, the spectra cover the entire optical spectrum from 3600 to 7000 Å over ~50 orders, although here we will discuss only the Hα and [O III] lines in detail. Spectra were obtained with a 2″ × 4″ slit and 2″ × 45″ slit along the southeast bright ridge of emission in N49. The small-aperture observation isolated the orders and permitted accurate order centering and wavelength calibration, which was accomplished from comparison with a Th-Ar lamp exposure. The long-slit observation provided much more spatial coverage at the expense of overlapping orders. Since we were mainly interested in emission lines, the blending due to order overlap was relatively minor. The orientation of the 45″ slit was the same as for LS1, sampling the brightest emission along the southeast ridge, and the integration time was 600 s. The spatial scale was 0″.5 pixel^{-1}, and the spatial resolution was between 2″.5 and 3″, corresponding to 0.6–0.75 pc. The two-dimensional image was flat-fielded, transformed to remove distortions, and background-subtracted. Figure 5 (Plate 6) shows a part of the resultant image, including lines of Hα, Hβ, and [O III] λ5007. Because of the high velocities in N49 and the overlapping orders, the [O III] λ5007 line and Hβ overlap somewhat. However, Hα and [O III] λ4959 are clear of overlap problems.

From Figure 5, both Hα and [O III] show a faint diffuse "ball" of emission of extent HWZI (half-width zero intensity) 230 km s^{-1}. Shull (1983), from long-slit echelle observations, along with Shull et al. (1985), have also found characteristic bulk speeds of ~200 km s^{-1} for [O III] and Hα in N49. Chu & Kennicutt (1988) report HWZI bulk velocities of ~280 km s^{-1} in Hα. These values appear to be constant with our data. Thus there is evidence for fast-moving shocks with velocities ≥200 km s^{-1}. In addition, as is most evident in Hα, there are bright emission bands whose wavelength centroids are offset from the line center and whose velocities are consistent with bulk motions ≤140 km s^{-1}. The bands imply structure on the scale of ~0.8 pc, an upper limit, since this is roughly the spatial resolution. Measurements reveal that roughly two-thirds of the total flux in Hα arises from the diffuse "ball" component, with one-third coming from the bands.

A third component to the line profiles, most evident in the [O III] lines but present in Hα as well, is a narrow "spike" of emission present along the entire length of the long slit. The velocity dispersion is less than 13 km s^{-1} in both Hα and [O III], and Shull (1983) has previously shown that this width is due mostly to thermal broadening, consistent with a shock wave precursor of temperature ~10^4 K.

Careful measurement reveals that the excess emission from the spike (i.e., excluding underlying emission) is ~18% of the total emission in [O III]. The same exercise with Hα yields ~5% of the total emission in the spike component. From the long-slit data, the average observed surface brightnesses in [O III] and Hα along the length of LS1 are 1.0×10^{-14} and 3.4×10^{-14} ergs cm^{-2} s^{-1} arcsec^{-2}, implying spike brightnesses of 1.8×10^{-15} and 1.7×10^{-15} ergs cm^{-2} s^{-1} arcsec^{-2}. Comparing these values with the nearby H II region surface brightness measurements of § 2.2, it is clear that any superpositioned H II region contributes little to the spike emission.

2.4. *IUE Observations*

Extensive *IUE* observations of N49 were carried out between 1989 May and 1990 May. These observations comprised pairs of SWP and LWP spectra at each of five positions, shown as A, B, C, D, and E in Figure 1*l*. An observing log is given in Table 5. The *IUE* large aperture was positioned using accurate astrometry and blind offsetting from a 9th magnitude star (SAO 249271) ~3′ to the southwest of N49. During each SNR exposure, the other *IUE* camera was exposed to sample nearby LMC background regions. Each pair of SWP and LWP SNR spectra, except for position B, have virtually coincident position angles.

IUE data reductions were performed using an IRAF–based *IUE* reduction package that we have developed, the results of which are essentially identical to Goddard Space Flight Center RDAF reductions. Using the line-by-line files on the guest observer tapes, we removed cosmic-ray "hits," reseaux marks, and known hot camera pixels, and reextracted the lines corresponding to SNR emission in addition to representative backgrounds from lines adjacent to the large aperture. The backgrounds were scaled to the same number of lines as SNR emission, smoothed, and then subtracted from the SNR data. The inverse sensitivity curves of Bohlin (1986) were then applied to convert to flux units. As an example, the extracted SWP and LWP spectra for position A are shown in Figure 6. There is a clear continuum in the SWP which we attribute to H two-photon continuum (see Benvenuti et al. 1980).

Line identifications and intensities for the *IUE* positions are given in Table 6. In all the SWP spectra, C IV λ1550 and He II

TABLE 5

IUE OBSERVATIONS OF N49

APERTURE POSITION[a]	DATE (UT)	IMAGE	COORDINATES		INTEGRATION TIME (minutes)	POSITION ANGLE
			α(1950)	δ(1950)		
A	1989 May 31	SWP 36372	$05^h26^m00^s.5$	−66°07′34″.8	403	60°
A	1989 Jun 1	LWP 15636	05 26 00.5	−66 07 34.8	418	60
B	1989 Jul 19	SWP 36706	05 25 59.6	−66 07 45.8	390	110
B	1990 May 30	LWP 18013	05 25 59.6	−66 07 45.8	395	60
C	1990 Feb 12	SWP 38183	05 25 56.9	−66 07 03.1	396	−46
C	1990 Feb 17	LWP 17388	05 25 56.9	−66 07 03.1	405	−41
D	1990 Feb 13	SWP 38186	05 25 59.4	−66 07 29.3	415	−45
D	1990 Feb 15	LWP 17372	05 25 59.4	−66 07 29.3	410	−43
E	1990 Apr 25	SWP 38676	05 25 55.0	−66 07 50.1	405	25
E	1990 Apr 26	LWP 17810	05 25 55.0	−66 07 50.1	420	26

[a] See Fig. 1*l* for aperture locations.

1992ApJ...394..158V

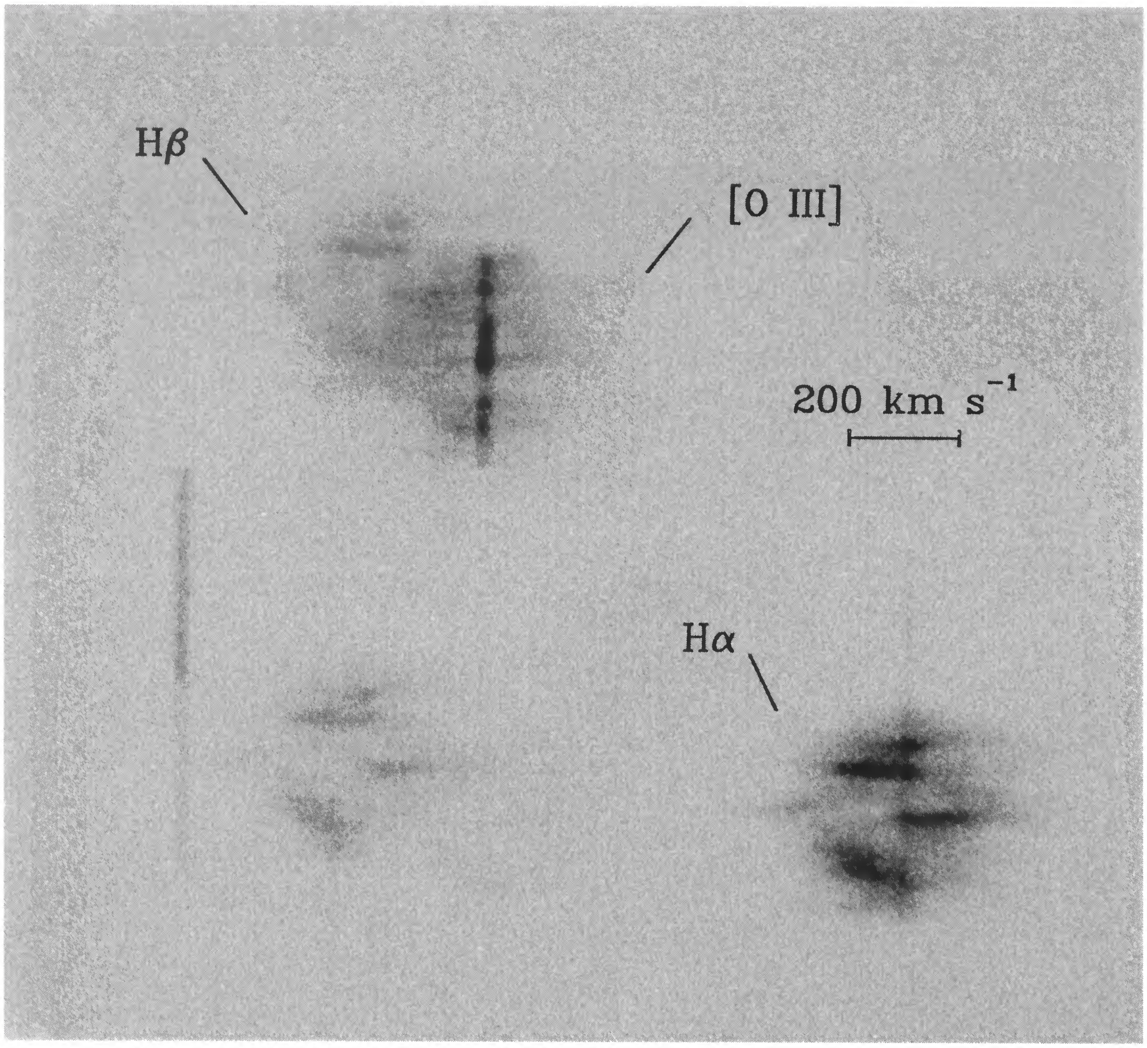

FIG. 5.—Two-dimensional echelle spectrum along the southeast ridge of N49. The northeast spatial direction is up. Wavelength is positive to the right. Note in particular the Hα and [O III] emission, consisting of broad bands, a narrow spike, and diffuse emission moving at bulk velocities ~200 km s^{-1}.

VANCURA, BLAIR, LONG, & RAYMOND (see 394, 164)

1992ApJ...394..158V

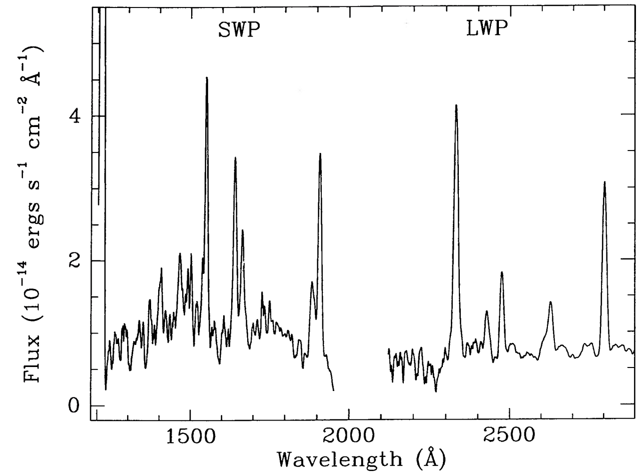

FIG. 6.—One-dimensional reduced *IUE* SWP and LWP spectrum of *IUE* position A. Note the two-photon continuum at shorter wavelengths as well as the appearance of the 2628 Å feature in the LWP range.

λ1640 are present, but N v λ1240 is noticeably absent. The values given for N v represent 2 σ upper limits, based on the root mean square of neighboring background regions. All of the features in our *IUE* spectra of N49 are associated with well-known emission lines except for the feature centered at 2628 Å which is apparent in the LWP exposures at positions A, B, and D. This feature is real, having the same extent as other spectral lines in the *IUE* data. During concurrent "serendipitous" exposures using the LWP camera, no distinctive instrument features were seen at or near 2628 Å. The presence of the feature in the spectra from three different positions argues against it being a "hit" due to a cosmic ray. This is the first observation of a line at this wavelength in a SNR, and its possible identification is discussed below and in the Appendix.

The UV extinction within the LMC has been a subject of debate. Fitzpatrick (1985) argued that the "average" LMC extinction curve (cf. Howarth 1983), based largely on stars from the 30 Doradus region, is not representative of the LMC as a whole. Since N49 is in the northern outskirts of the LMC, the 30 Dor curve may not be appropriate. We adopt a representation of Fitzpatrick's "non–30 Dor" curve, taken to lie one-third of the way from the $A(\lambda)/E(B-V)$ Galactic curve of Seaton (1979) to the LMC curve of Howarth (1983). For positions A, B, and C, the values of $E(B-V)$ derived from the counterpart optical spectra at these locations were applied to the Fitzpatrick "non–30 Dor" curve under the assumption that the bulk of the extinction is intrinsic to the LMC. For positions D and E, the average value of $E(B-V) = 0.37$ was used. For position A, using the Tucker & Koren (1971) two-photon spectral shape and the fluxes measured in the 1280–1380, 1420–1500, and 1700–1800 Å bands, we estimate the total intrinsic two-photon flux to be 2.3×10^{-10} ergs cm^{-2} s^{-1}, assuming $E(B-V) = 0.35$.

As can be seen from the optical images, the *IUE* positions generally sample regions of high optical surface brightness. However, *IUE* SWP position B was chosen so that the long dimension of the aperture sampled not only the bright optical emission in the southwest but also radially outward to the X-ray edge of N49 (including the bright [O III]:[O I] ridge). Close inspection of the line-by-line file indicates that the UV emission closely tracks the bright optical flux, abruptly cutting off ($\leq 2''$) at the outskirts of the optical clouds. Hence, the high-ionization UV lines such as C IV and He II do not appear to extend radially outward from the bright optical filaments. At all five positions, the line-by-line files indicate that the bulk of the UV emission is closely associated with bright optical emission.

3. ANALYSIS

3.1. *Densities and Temperatures in the Optical Filaments*

The rich optical and IR spectral region allows us to analyze physical conditions in parts of the recombination flow. Using the ratio of the [S II] λλ6717, 6731 lines, we may obtain the electron density in the S^{+1} region of the recombination zone (cf. Osterbrock 1989). Assuming $T_e \simeq 10^4$ K yields $\langle n_e \rangle \simeq 1.8 \times 10^3$ cm^{-3} and 1.0×10^3 cm^{-3} along the entire slits LS1 and LS2, respectively. The variation of electron density along each of these slits is very small. At each position along LS1 and LS2,

TABLE 6

IUE OBSERVED AND DEREDDENED FLUXES

	A		B		C		D		E	
LINE	$F(\lambda)$	$I(\lambda)$	$F(\lambda)$	$I(\lambda)$	$F(\lambda)$	$I(\lambda)$	$F(\lambda)$	$I(\lambda)$	$F(\lambda)$	$I(\lambda)$
N v λ1240	<8.3	<16.8	<8.4	<18.3	<19.0	<53.2	<8.3	<17.3	...	...
O IV] λ1402	22:	28:	25:	32:	51	71	13:	17:	7:	9:
C IV λ1550	100	100	100	100	100	100	100	100	100	100
He II λ1640	88.8	80.4	58.4	52.3	96.9	84.0	87.7	79.0	47.3	42.7
O III] λ1663	58.7	52.1	51.0	44.6	57.1	48.1	29.0	25.6	38.1	33.6
Si III] λ1892	75.7	65.4	38.0	32.2	...	...	122	104	44.0	37.8
C III] λ1909	124	108	90.3	77.8	96.9	80.0	145	125	67.3	58.3
C II] λ2325	163	147	163	145	127:	108:	170	152	75.3	67.1
[Ne IV] λ2423	32.2	22.6	28.8	19.4	...	...	26.6	18.2	...	...
[O II] λ2470	56.2	35.9	44.0	26.5	...	...	64.2	39.8	28.6	17.7
[Ti III]?[a] λ2628	47.1	23.5	27.1	12.5	...	...	39.6	18.9	...	...
Mg II λ2800	128	53.9	131	50.0	113	32.0	157	62.5	48.2	19.2
C IV λ1550[b]	3.29	56.7	3.61	86.3	0.98	62.1	2.93	59.5	3.36	68.2
$E(B-V)$[c]	0.35		0.39		0.51		0.37		0.37	

[a] The possible identifications of this line are discussed in the text.

[b] F(C IV), I(C IV) in units of 10^{-13} ergs cm^{-2} s^{-1}. C IV fluxes equal 100 in units of the table.

[c] Reddening values assumed from optical data; see text.

1992ApJ...394..158V

the [S II] ratio varies by less than 10% from the average, with the exception of an anomalous knot of emission in the north along LS2 ($n_e \simeq 1.8 \times 10^3$ cm^{-3}). For LS3, which lies roughly along a diameter of N49, the density varies appreciably, bounded by the densities given for LS1 and LS2 above. These results strongly suggest that densities of optically emitting filaments are higher in the southeast by a factor of roughly 2.

Ions such as O^{+2}, N^{+1}, and C^0 can be used to calculate electron temperatures for regions in which these ions reside. However, N^{+1} and C^0 temperatures are seldom derived because of the faintness of the auroral transitions and the relatively few observations of SNRs out to ~ 1 μm (for C^0). The brightness of N49's filaments coupled with the good sky subtraction available in the long-slit spectra makes it possible to determine these temperatures as follows.

The densities calculated above for the [S II] region in N49 are sufficiently low that C^0 and N^{+1} are in the low-density limit. Treating the lowest ^3P, ^1D, and ^1S states as a five-level system where collisional excitations are responsible for the upper-level populations and solving for the ratio of fluxes emitted between the ^1D and ^3P levels and ^1S and ^1D levels yields, with collision strength $\Omega(T)$, transition rate A, and energy difference between levels ΔE,

$$\frac{I_{^1D,^3P_1} + I_{^1D,^3P_2}}{I_{^1S,^1D}} = \left[\frac{\Omega(T)_{^3P,^1D}}{\Omega(T)_{^3P,^1S}}\,\alpha^{-1}\exp\left(\frac{\Delta E_{^1S,^1D}}{kT}\right) + 1\right]\beta\,, \tag{1}$$

where

$$\alpha = \frac{A_{^1S,^1D}}{A_{^1S,^1D} + A_{^1S,^3P}}\,, \quad \beta = \frac{\lambda^{-1}_{^1D,^3P_2} A_{^1D,^3P_2} + \lambda^{-1}_{^1D,^3P_1} A_{^1D,^3P_1}}{\lambda^{-1}_{^1D,^1S}(A_{^1D,^3P_2} + A_{^1D,^3P_1})}\,.$$

Using the values for A and $\Omega(T)$ of Drake (1971) and Eissner & Zeippen (1981), as compiled by Mendoza (1983), solving equation (1) for T, and inserting parameters for C^0, we infer temperatures of 9.1×10^3 and 8.0×10^3 K for the entire slit LS1 and the extraction corresponding to *IUE* position A, respectively. The errors on these temperatures are dominated by the incomplete subtraction of the OH band slightly redward of 8730 Å and the subsequent uncertainty in the measurement of [C I] λ8730. Assuming an error of $\sim$30% for λ8730., we estimate an uncertainty of 2×10^3 K. These are the first measurements of the temperature in the C^0 zone of a SNR.

For [N II] we obtain temperatures of 1.3×10^4 and 1.2×10^4 K for the entire slit LS1 and *IUE* position A, respectively. Differences ($\sim 2 \times 10^3$ K) in temperature along the slit are primarily due to uncertainties in the measurement of the 5755 Å line. Because of the faintness of this line, we were unable to determine temperatures from the [N II] lines along the slits LS2 and LS3.

3.2. *Comparison with Shock Models*

As a shock becomes fully radiative, much of the original "character" (velocity and preionization) of the shock is "forgotten." Each part of the recombination flow radiates away a fixed fraction of the total thermal energy, and relative changes of intermediate ionization line strengths reflect abundances rather than physical conditions at the shock front (see, e.g., Benvenuti, D'Odorico, & Dopita 1979; Dopita et al. 1984). Cox & Raymond (1985) have developed families of radiative shocks whose members have different velocities and preionization states but downstream lead to the same spectra.

Although lines of low and intermediate ionization are found both optically and in the UV, the UV is also home to high-ionization species, emitting lines such as C IV, N V, and O VI $\lambda\lambda$1032, 1038. Since postshock temperature is proportional to the square of shock velocity, a given velocity constrains the maximum postshock temperature and ionization structure. Emission from high-ionization species in a shock wave can thus place tight bounds on the actual shock velocity (cf. Blair et al. 1991a). The UV spectral region, therefore, has more memory of the initial shock conditions and can be used to sample the shock front itself.

In order to interpret the observations of N49, we have calculated models of radiative shocks using Raymond's (1979) code with revisions discussed in Cox & Raymond (1985). We have updated the collision strengths for hydrogen based on the calculations of Giovanardi, Natta, & Palla (1987), since we want to investigate whether shock models appropriate for N49 produce a Balmer decrement equal to 3.0. We have made several "global" assumptions in running the code. For all shocks, complete ion-electron temperature equilibration was assumed. The preshock temperature is 10^3 K, and we have terminated all models when the postshock temperature drops to 10^3 K. We have chosen the preshock neutral fractions to approximate the equilibrium preionization case: for shock velocities less than 80 km s^{-1}, the incident H and He are assumed neutral. For velocities between 80 and 100 km s^{-1} inclusive, we have adopted the equilibrium ionization fractions of Shull & McKee (1979). For velocities between 100 and 180 km s^{-1}, we have assumed complete single ionization of H and He; for shock speeds equal to or greater than 180 km s^{-1}, He is also assumed to be fully ionized.

We wish to find a set of abundances and a distribution of shock velocities which result in spectra that match the data. To clarify the following discussion, we briefly outline our strategy. We began by constructing a grid of models (in velocity space) assuming the N49 abundances of Russell & Dopita (1990), a negligible magnetic field of 0.1 μG, and ram-pressure equilibrium. We fixed the shock velocity of 100 km s^{-1} to a preshock density of 30 cm^{-3}. The analysis of this output revealed that a distribution of shock velocities was necessary to match the observations. The analysis also suggested several changes to our input parameters. Using the UV C II]:O II] and C III]:O III] lines, we decided to raise the C abundance by a factor of 3. To match our observed luminosities of Table 2, we raised the preshock densities by a factor of 5. To keep the predicted [S II] densities close to their observed values, we employed a preshock magnetic field in order to provide postshock nonthermal support. We then ran a second set of models. By considering lines of the major coolants H, O, and C, we found a suitable distribution of shock velocities that matched the observations. We finally adjusted the abundances of the minor coolants to bring their lines into agreement with the observations.

Since *IUE* position A is representative of the remnant as a whole, we shall compare the observations at this position with the models. Table 7 reproduces the observational results presented in Tables 4 and 6, with two important differences. We have subtracted the contribution to [O III] from shock precursors (Shull's [1983] "spike" component), since the models are not designed to replicate the preshock emissions. Also, we have raised the N V, C IV, and Mg II fluxes by one-third to account for LMC absorption. The profiles of these absorption lines seen in LMC stars (cf. Savage & de Boer 1981; Dupree et al. 1987) suggest that a large fraction of the emission blueward of the rest velocity (in the LMC frame) will be absorbed. Hence, a

TABLE 7

Comparison of Observations to Model Shock Waves

	Observed[a]	Ia	IIa	IIb	IIc	III	IV	V
V_s		110	110	40	150	60,120	40-270	40-270
Abundance[b]		RD	RD*	RD*	RD*	RD*	RD*	VBLR
N V λ1240	<16.8	1	0	0	35	1	17	20
O IV] λ1402	21	51	17	0	71	17	44	44
C IV λ1550	100	100	100	0	100	100	100	100
He II λ1640	60	30	10	0	14	11	14	20
O III] λ1663	39	123	35	0	42	29	39	39
Si III] λ1892	49	172	46	0	32	30	52	49
C III] λ1909	81	119	102	0	50	76	82	82
C II] λ2325	111	57	53	100	35	46	63	63
[Ne IV] λ2423	17	33	10	0	30	10	22	17
[O II] λ2470	27	24	10	1	8	8	13	13
Mg II λ2800	54	136	54	340	54	58	93	54
2-γ	3120	422	138	7300	108	776	975	975
Hβ λ4861	100	100	100	100	100	100	100	100
[O III] λλ4959,5007	140	516	456	0	444	141	138	138
[N I] λ5200	3.0	41	25	54	19	12	15	18
[Fe III] λ5270	3.5	14	13	0	12	4	5	3
He I λ5876	11	23	22	0	16	7	7	11
[O I] λλ6300,6363	120	271	224	287	186	115	125	125
[N II] λλ6548,6584	89	139	153	10	164	66	75	89
Hα λ6563	300	298	296	396	291	308	308	308
He I λ6678	2.8	7	6	0	5	2	2	3
[S II] λ6717	90	176	105	185	92	48	63	93
[S II] λ6731	121	200	149	154	135	67	80	118
[Ar III] λλ7136,7752	5.1	23	23	0	18	7	8	5
[Ca II] λλ7292,7325[c]	34	72	55	34	55	22	27	34
[O II] λλ7322,7332[c]	28	59	70	1	61	22	29	29
[Fe II] λ8617	14	76	65	69	58	32	36	18
[S III] λλ9069,9532	17	115	136	1	109	62	55	80
[C I] λ9823,9850	7.9	98	101	174	91	78	74	74
Hβ λ4861[d]		6.6E-5	3.1E-4	6.4E-5	3.8E-4	2.8E-4	2.5E-4	2.5E-4
C IV λ1550[d]		1.2E-4	1.7E-3	4.9E-5	2.1E-3	5.9E-4	4.2E-4	4.2E-4

[a] Observations are taken from Tables 4 and 6 at *IUE* position A (see text for corrections). Because of uncertainties in reddening and aperture-size scaling factors, fluxes are given relative to Hβ = 100 and C IV = 100.

[b] The assumptions made in running the models are discussed in the text. RD corresponds to the abundances of Russell & Dopita 1990. RD* has the C abundance raised by a factor of 3. The final column employs abundances derived in this paper.

[c] The [Ca II] $\lambda7325$ line is take to be $\frac{2}{3}$ the strength of the $\lambda7292$ line from Table 4. The remaining emission in the $\lambda7325$ blend comprises [O II].

[d] The model fluxes in these lines are given in ergs cm^{-2} s^{-1} through the front of the shock. Fluxes are in units equivalent to those used for the observed data (except for model IIb, whose UV fluxes are relative to C II]).

factor of 2 is the maximum correction expected, but the line of sight to N49 should be less affected than the line of sight to objects near 30 Dor. Absorption by the Galactic halo (cf. Savage & de Boer 1981) is less significant than the spatially varying absorption intrinsic to the LMC. Because of the large reddening variations, uncertainty in UV extinction curve, and differing aperture sizes between UV and optical observations, we have chosen to scale the UV lines to C IV = 100, and the optical lines to Hβ = 100.

The first grid of models was run with the N49 abundances of Russell & Dopita (1990) ("cosmic" He and Mg abundances): He:C:N:O:Ne:Mg:Si:S:Ar:Ca:Fe equal to 10.93:7.66:7.40:8.54:7.95:7.12:7.48:7.00:6.65:6.30:7.30. We adopted a negligible magnetic field ($B = 0.1$ μG). With no magnetic field present, the observed [S II] densities suggest preshock densities of roughly 30 cm^{-3} for shock velocities of 100 km s^{-1} (cf. Dopita 1979). We adopted these values and assumed that the main blast wave drives shocks of differing velocities but equal ram pressures $\rho_0 v^2$ into regions of different densities. A grid of models from 20 to 180 km s^{-1} with 10 km s^{-1} differential in velocity space was constructed. In Table 7 we show the predicted emission from a "typical" radiative shock of 110 km s^{-1} with a gas density of 24.8 cm^{-3}, listed as model Ia. For all models, the fluxes listed for Hβ and C IV represent emission through the front of the shock (i.e., 50% of the total emission).

Some general comments on this first set of models are warranted: N V, C IV, and O III] (or [O III]) have "turn-on" velocities of roughly 140, 110, and 100 km s^{-1}, respectively. For shocks with velocity ≥ 110 km s^{-1}, [O III]:Hβ ~ 5.3, while [O I]:Hβ ~ 2.7. For shocks of velocity ≤ 80 km s^{-1}, there is virtually no [O III] produced, while [O I]:Hβ is roughly 0.5, although [O I]:Hβ rises rapidly (by orders of magnitude) for shocks ≤ 50 km s^{-1}. Shocks of at least 110 km s^{-1} must be prevalent to produce the observed C IV $\lambda1550$. N V is not detected, however; therefore, most of the C IV arises in shocks with velocities between 110 and 140 km s^{-1}. Appreciable numbers of faster shocks may be present if the N abundance is much smaller, but this is unlikely, since the [N II]:Hα ratio is reasonable.

Comparison of the shock models with the data immediately reveals that a single shock velocity cannot be reconciled with any combination of abundances. From Table 7, the observed [O III]:[O I]:Hβ ratio is 1.4:1.2:1, while the predicted

[O III]:[O I]:Hβ for shocks ≥ 100 km s^{-1} is roughly 5:2.5:1. Changing the abundance of O changes the fluxes of [O III] and [O I] with respect to Hβ, but little with respect to each other. Thus bringing down the O abundance to match [O III]:Hβ requires the existence of extremely slow shocks (≤ 40 km s^{-1}) which produce prodigious [O I] and relatively little Hβ and [O III]. On the other hand, if we lower Z(O) only somewhat or not at all, we must appeal to shocks between 50 and 90 km s^{-1} to bring up [O I]:[O III] while adjusting both [O I] and [O III] down relative to Hβ. In either case, there must be significant mixing with shocks of velocities less than 100 km s^{-1}.

Upon comparing predicted luminosities with those of Table 2, we find a severe problem with our assumptions for this first set of models. Assuming the shock described by model Ia to cover the entire surface of a 9 pc radius sphere representing N49, we find that the predicted Hα and [O III] luminosities are only 15%–40% of those measured. (Note that the inferred [O III] postshock luminosity from Table 2 is roughly 1.5×10^{37} ergs s^{-1}, after taking into account the addition of the line λ4959 and subtraction of the precursor emission.) We are forced to the following conclusions. The average preshock density must be several times higher in order to match the observed luminosities. This suggests that magnetic fields (or other nonthermal pressure sources) are present to keep the density in the postshock flow low enough to match the observed [S II] line ratios. Though cosmic rays may also contribute to nonthermal pressure (cf. Raymond et al. 1988), in the second grid we have employed solely magnetic fields in this regard. We have scaled the preshock field linearly with the preshock density so that the maximum postshock density remains constant (with $\rho_0 v^2 =$ constant, as we have assumed). The effects of a higher density compensated by magnetic pressure are subtle. The major effect is an increase in the photon flux relative to the particle density in the recombination zone. This tends to weaken the lines of neutral species, particularly C^0.

The intermediate-ionization UV C III]:O III] and C II]:O II] ratios reflect the relative carbon and oxygen abundances rather than shock velocity. The first set of models suggests a factor of 3 increase in C relative to O. In the second set of models, we have chosen to increase the C abundance by 3, while keeping Z(O) fixed. Observable C lines fall either in the UV or IR, while O has several optical lines, which leads us to believe that the C abundance determination is more uncertain. Russell & Dopita (1990) assumed that only 150 km s^{-1} shocks are responsible for all the emission, but we have shown that a distribution of shock velocities is necessary. For a 150 km s^{-1} shock the predicted emission relative to Hβ will be too high because contributions from slower shocks (with lower emissions relative to Hβ) are neglected. The inferred elemental abundances will then tend to be too low, and this makes us loath to diminish Z(O). Another problem with decreasing the O abundance is that it requires still higher preshock densities to match the observed [O III] luminosity. Lowering Z(O) would also necessitate a greater contribution from slow (≤ 40 km s^{-1}) shocks in order to match the observations. We avoid an excessive appeal to these very slow shocks, since their neutral emissions are extremely sensitive to magnetic field strength.

The second grid of models ran from 40 to 270 km s^{-1} in velocity space, with a spacing of 10 km s^{-1}. For this grid, we raised the C abundance by a factor of 3 and anchored the shock velocity of 100 km s^{-1} and preshock B field of 15.7 μG to a density of 150 cm^{-3}, under the requirement that $\rho_0 v^2$ and ρ_0/B remain constant. The implied densities and magnetic fields range from approximately 20 to 940 cm^{-3} and 2 to 98 μG, respectively. The lower bound to the shock velocity grid is dictated by the Alfvén speed, while the higher preshock density implies that faster shocks are now also capable of becoming radiative (see discussion in § 4).

Previously, several authors have argued for the influence of nonthermal pressure support in shock evolution. Blair, Kirshner, & Chevalier (1981) suggest that magnetic fields may be responsible for the correlation between SNR explosion energy and diameter as seen in extragalactic surveys. Raymond et al. (1988) demonstrate that postshock thermal pressure in the Cygnus Loop "spur" filament is only a fraction of the ram pressure. They report that *if* magnetic fields are solely responsible for the postshock nonthermal support, then preshock B fields of 15 μG (preshock density ~ 8 cm^{-3}) must exist. With our parameters, the strength of the postshock magnetic field approaches 10^{-3} G, which, though large, is reasonable given the high preshock densities that we are invoking.

To compare the new results with the old, we present the results for the 110 km s^{-1} shock in Table 7 as model IIa. When compared with model Ia, the C lines have increased by about a factor of 3 relative to the other UV lines. The C IV flux relative to Hβ has also tripled, and the Hβ flux has increased several fold, due to the higher preshock density. The relative strengths of the neutral and [S II] lines have decreased. For [S II] the line λ6717 has dropped primarily because of the density increase, and the λ6731 reduction is caused by the inclusion of magnetic fields. For comparison we present the 40 and 150 km s^{-1} shock predictions as models IIb and IIc, respectively. Model IIb, as expected, is devoid of high-ionization lines, while in model IIc, N V has reached a strength comparable to that of C IV. Model IIa is the best single velocity fit to the data. However, there are still striking disagreements. In particular, the O lines cannot be made to agree with the observations, even with changes in abundance.

We have explored the possibility that a superposition of two shock velocities will explain the observed line intensities. We obtain a satisfactory parameterization of the data from a combination of shocks at 60 and 120 km s^{-1} in a surface area ratio of $\sim$3:1. The two distinct shock velocities imply different preshock densities. The predicted fluxes are given as model III in Table 7. For model III, the lines [O I], [O II], and [O III] in the optical match the observations, while O IV], C IV, O III], and C III] in the UV remain correlated. The high-ionization lines arise mostly from the 120 km s^{-1} shock, while both shocks contribute to the optical lower ionization lines. Model III appears to be the simplest distribution of velocities that matches the emission from the wide range of postshock ionization states observed.

That two distinct shock velocities give rise to all the optical emission is certainly only an approximation to a more complicated situation. The ISM density distribution is likely to be more continuous, implying a broad distribution of shock velocities. On the global scale of the SNR there exist slow, optical shocks, fast $\sim$200 km s^{-1} shocks seen in the echelle spectra, and nonradiative X-ray–emitting shocks ≥ 400 km s^{-1}, which all arise from the same local ISM. We have therefore modeled the observed fluxes with a power-law velocity distribution. In terms of the relative H, C, and O line intensities, model IV of Table 7 is the result of the best fit to the *entire* range of second grid velocities, with constant ram pressure. For model IV, the area A covered by shocks with velocity V is $A(V) \propto (V/100)^p$, with $p = -2.20$. Aside from its aesthetic advantage, this power law also seems to be the best fit to the data. It brings the [O II] and O III] lines into closer agreement with the observations. It also raises the two-photon continuum level, although for slow shocks the two-photon continuum flux is an extremely sensitive function of magnetic field and shock velocity.

We now turn to the abundances of the other elements, which we derive by scaling abundances linearly to match the observations, if possible. Thus, from model IV our final abundances for He:C:N:O:Ne:Mg:Si:S:Ar:Ca:Fe are 11.13:8.14:7.47:8.54:7.84:6.88:7.45:7.17:6.45:6.40:7.00. We present the final power-law spectrum with these abundances as model V in Table 7. It should be kept in mind, however, that the N, Mg, Si, Ar, and Ca abundances are derived from lines of just one ion. The C:O ratio is probably reliable because four ions of each element are observed.

A major discrepancy is that the [C I] lines in the IR are significantly overpredicted. The C^0 ionization in the recombination zone is dominated by photoionization from the ^1D metastable level by Lyα photons. The model does not include Lyα trapping by resonant scattering, but we expect that trapping greatly increases the local Lyα intensity and decreases the neutral carbon population and [C I] emission. This would have the additional benefit of increasing the [C II] emission, which is predicted too weak. The other significant discrepancy is the overprediction of [S III]. The only way we see to reconcile the [S II] and [S III] intensities is an increase in the S^{+2} recombination rate and a modest decrease in the sulfur abundance. Charge transfer with neutral hydrogen is negligible (Christensen & Watson 1981). Low-temperature dielectronic recombination does not appear promising either. Badnell (1991) only gives dielectronic recombination rates above 30,000 K, but these rates appear unlikely to be large at the lower temperatures relevant to the [S II]:[S III] line ratio.

Our derived abundances differ from those of Russell & Dopita (1990) by factors ≤ 3, and the abundances of the coolants C, N, and O are either equal to or greater than those of Russell & Dopita, as might be expected from the above discussion. Except for Si, Ar, and Fe, our elemental abundances are higher than the average LMC SNR abundances of Russell & Dopita. Our derived C and O abundances are close to those inferred from H II regions (Dufour 1984), but other elemental species do not share similar agreement. In particular, our Z(N) is a factor of 3 higher than that inferred from the H II regions. This trend is seen for SNRs and H II regions in other nearby galaxies (Blair & Kirshner 1985; Blair, Kirshner, & Chevalier 1982) but is not entirely understood.

There are several reasons why our derived abundances disagree with those of Russell & Dopita 1990. First, we are using a different shock modeling code. Second, in Russell & Dopita, there appear to be some inconsistencies in the predicted O emission versus abundance for the LMC remnants. Observationally, Russell & Dopita do not correct for LMC extinction of the UV resonance lines which introduces additional error. Russell & Dopita use a smaller extinction correction to deredden their spectra, finding an intrinsic Balmer decrement of 4.4:1 for Hα:Hβ. We note that, in order to substantially change Hα:Hβ, shocks with $V_s \leq 50$ km s^{-1} are required. For example, model IIb indicates a Balmer decrement of roughly 4. Although there clearly appears to be a range of shock velocities, there do not appear to be enough slower shocks to appreciably enhance the Balmer decrement. In particular, the best-fitting models III and IV in Table 7 show a Balmer decrement of roughly 3:1, suggesting that the assumed Hα:Hβ ratio of § 2 is appropriate and the extinction variations indicated there are real. Because abundances are determined by matching lines relative to Hβ, a smaller extinction correction results in underestimating the abundances of elements whose lines lie blueward of Hβ, and overestimating those whose lines are redward of Hβ. On the other hand, the assumptions made by Russell & Dopita that a single shock velocity of 150 km s^{-1} accounts for all the emission, and that the preshock magnetic field is negligible, are clearly not valid. Because our range of shock velocities and preshock magnetic fields is more representative of actual conditions in N49, and because our final predicted spectrum also more closely matches the observations, our abundances should be more accurate.

We can use the models to achieve an independent, albeit uncertain, measurement of the reddening to N49. The predicted ratio of [O III] $\lambda\lambda$4959, 5007 to O III] λ1663 is $\sim$2.2 for shock velocities $\leq$140 km s^{-1}. This yields an alternative measure of the extinction, and we derive $E(B-V) = 0.51 \log(0.45F_{[\mathrm{O\,III}]}/F_{\mathrm{O\,III}]})$. From the [O III] image of 1e, we have obtained the inferred "spike"-subtracted [O III] flux of *IUE* position A. This and the observed O III] flux from Table 6 yield $E(B-V) = 0.34$ at *IUE* position A. It is comforting though possibly somewhat fortuitous that this value of the reddening so closely matches that in Table 4A, given the uncertainty in the image fluxes and the spatial reddening variations within the different apertures. We have also separately summed all the *IUE* O III] emissions and the corresponding [O III] image sections. The same procedure outlined above yields a global $E(B-V) = 0.33$, which is reasonably close to the average value derived from the Balmer lines.

We next estimate the total fluxes in these *IUE* UV lines. To obtain total luminosities, we adopt a procedure similar to that described in Blair et al. (1991b) for *Voyager* observations of the Cygnus Loop. The flux in the [O III] map associated with all the *IUE* apertures is 5.8×10^{-12} ergs cm^{-2} s^{-1}, corresponding to 41% of the total. Under the assumption that the UV lines are produced in the regions producing [O III], we scale the total observed *IUE* emission by the inverse, 2.41, to obtain integrated fluxes in these UV lines. We have again increased the N V, C IV, and Mg II fluxes by 33% to account for LMC absorption. With $E(B-V) = 0.37$, the implied intrinsic total luminosities for the UV lines are given in Table 8. The preferential propagation of emission from regions with low reddening is much more pronounced in the UV than in the optical. Dereddening accomplished with the use of an optically derived extinction value will overestimate the intrinsic UV line strengths. This effect dominates the correction for extinction bias. Hence, the luminosities listed in Table 8 will tend to be overestimates. However, we have calculated these effects for various spatial reddening distributions. For any reasonable distribution of reddening values, we find the effect to be $\leq$33% for O IV] and $\leq$25% for all other detected *IUE* lines. The luminosities of Table 8 are comparable to both the optical luminosities given in Table 2 and the X-ray luminosity given by Long et al. (1981).

The total luminosity in C IV that we report for N49 is a factor of 7 greater than that reported by Blair et al. (1991b) for the Cygnus Loop. Blair et al. could not determine whether the C IV emission in the Cygnus Loop was associated more closely with C III λ977 or with O VI $\lambda\lambda$1032, 1037. It might be expected

TABLE 8

INFERRED UV TOTAL OBSERVED FLUXES AND TOTAL INTRINSIC LUMINOSITIES[a] OF N49

Line	$F(\lambda)$ (ergs s^{-1} cm^{-2})	$L(\lambda)$ (ergs s^{-1})
N V	$<4.0 \times 10^{-13}$	$<5.1 \times 10^{36}$
O IV]	6.6×10^{-13}	5.3×10^{36}
C IV	4.5×10^{-12}	2.8×10^{37}
He II	2.4×10^{-12}	1.3×10^{37}
O III]	1.6×10^{-12}	8.4×10^{36}
Si III]	2.2×10^{-12}	1.1×10^{37}
C III]	3.6×10^{-12}	1.9×10^{37}
C II]	4.8×10^{-12}	2.6×10^{37}
[Ne IV]	7.0×10^{-13}	2.9×10^{36}
[O II]	1.5×10^{-12}	5.7×10^{36}
[Ti III]?	8.9×10^{-13}	2.6×10^{36}
Mg II	5.2×10^{-12}	1.3×10^{37}

[a] Assumes $E(B-V) = 0.37$ and a distance of 50 kpc to N49. See text for derivation.

a priori that the C IV emission would closely track the O VI, since both C^{+3} and O^{+5} are high-ionization lithium-like ions. However, we have demonstrated that for N49, although there exist ~200 km s^{-1} shocks capable of producing O VI, the bulk of C IV is associated with optical emission from slower shocks incapable of O VI production.

Finally, the models also confirm that the faint "ball" of emission seen in the echelle spectra cannot be due solely to complete shocks with velocities ≥ 200 km s^{-1}. If these shocks produced Hα comparable to that from the slower radiative filaments (§ 2.3), copious N V emission comparable to C IV is inescapable. A range of slower shock velocities is thus necessary to explain the "ball." Most of this diffuse echelle emission comes from shocks with velocities similar to those associated with the bands, producing very little N V. Therefore, the very fast shocks producing N V must cover too small an area to be observed in this line.

3.3. *Spectral Identifications*

3.3.1. *The* 2628 Å *Feature*

The feature at 2628 Å in the *IUE* data has not been identified previously in SNR spectra. This feature may be comprised of two lines, a stronger feature at 2628 Å with a weaker one at ~2607 Å. We have reexamined an unpublished *IUE* spectrum of the LMC SNR N63A from the archives (LWR 10182) and find a similar feature at 2628 Å.

We have searched extensively for possible identifications of this feature without finding one that is entirely satisfactory (see Appendix). From a list of candidates including Fe II, [Mg VII], Cr III, and [Ti III], we believe [Ti III] λ2628 to be the most likely possibility. However, there are two problems associated with the [Ti III] identification. [Ti III] cannot account for the weaker feature at 2607 Å, but the reality of this line and its association with the 2628 Å feature is unclear. Also, the cosmic abundance of Ti is a factor of ~300 lower than Fe, and ~5 lower than Cr.

If the 2628 Å feature is due to Ti, other lines should be observable. A confirmation of our hypothesis would be the observation of lines from the $3d4s\,^3D \rightarrow 3d^2\,^3P$ transitions. Although these transitions are also forbidden, they are the only other downward triplet transitions available to the $3d4s\,^3D$ upper state responsible for the 2628 Å line. Using data from Martin, Fuhr, & Wiese (1988), we estimate that the intrinsic line strengths (in energy units) at 3609 and 3639 Å should each be $\sim\frac{1}{8}$ the strength of the 2628 Å feature. Coupled with an $E(B-V)$ of 0.37, the expected observed energetic flux at either 3609 or 3639 is $\sim\frac{1}{4}$ the strength of the observed 2628 Å blend, or 2.5×10^{-16} ergs cm^{-2} s^{-1} arcsec^{-2}. This is a brightness within reach of modern detectors.

3.3.2. *The* 6100 Å *Continuum Emission*

We believe the sources of the emission seen in the 6100 Å continuum image are H and He recombination and two-photon continua. The only apparent line emission in the bandpass is weak [Fe VII] λ6085, unable to account for the flux listed in Table 2. From the images, we have measured fluxes in the Hα and 6100 Å filters corresponding to *IUE* position A. The observed and dereddened fluxes are 5.4×10^{-12} and 1.2×10^{-11} ergs cm^{-2} s^{-1} for Hα, and 2.2×10^{-13} and 5.2×10^{-13} ergs cm^{-2} s^{-1} for the 6100 Å filter. We take the H and He continuum emission coefficients to be 5.1×10^{-29} and 6.4×10^{-29} ergs cm^3 s^{-1} Å^{-1}, respectively, at a temperature of 10^4 K. The Hα recombination coefficient is 3.5×10^{-25} ergs cm^3 s^{-1}. Setting the volume emissivities of H and He continuum emission and Hα recombination emission to be equal, we find that the expected continuum emission due to H and He recombination is only 1.9×10^{-15} ergs cm^{-2} s^{-1} Å^{-1}, or 2.5×10^{-13} ergs cm^{-2} s^{-1} for the entire bandpass. The remaining emission is two-photon continuum. For *IUE* position A, the total intrinsic two-photon flux of § 2.4, together with the spectral shape of Tucker & Koren (1971), yields a predicted two-photon flux through the bandpass of 3.6×10^{-13} ergs cm^{-2} s^{-1}. Thus the sum of expected two-photon and H and He continuum recombination emission is within 20% of the flux measured through the 6100 Å bandpass filter. At 6100 Å, the strength of the recombination continuum emission coefficient is roughly an order of magnitude greater than that for recombination two-photon continuum (cf. Osterbrock 1989). The relative strength of the two-photon continuum suggests a collisional excitation mechanism (see Dopita, Binette, & Schwartz 1982) and argues for the existence of slow shocks encountering neutral material, as presented in § 3.2.

3.3.3. *The Rings in the* [O III]:[O I] *and* [O III]:Hα *Maps*

The average surface brightnesses in [O III] and Hα in the regions where the [O III]:[O I] map (Fig. 2*d*) shows the enhanced outer ridge are 1.8×10^{-15} and 3.4×10^{-15} ergs cm^{-2} s^{-1} arcsec^{-2}. These figures, coupled with the values presented in § 2.3, suggest that most of the [O III] and one-half of the Hα emissions in the bright rings are due to shock photoionization precursors. The remaining emission is due to fainter radiative shocks, whose [O III]:Hα ratio is very close to the average for LS1.

The possibility that the enhanced [O III]:[O I] ring is due entirely to radiative shocks in the 100–140 km s^{-1} range, where [O III]:[O I] and [O III]:Hα are intrinsically higher, cannot be ruled out. However, from comparison with our LMC abundance models, the observed [O III]:Hα ratio appears to be too low by a factor of several for this to be the case. Moreover, this would imply that along much of the periphery of optical emission, the main blast wave is no longer encountering the densest clouds, which seems unlikely. Another possibility is a superposition of complete and incomplete shocks. However, for a cloud density of 50 cm^{-3}, the time scales during which incomplete shocks exist (Raymond et al. 1980; § 4), along with the observed radial extent of this ring (~0.5 pc), imply an uncomfortably large blast wave velocity of

$\sim 2 \times 10^3$ km s^{-1}. Larger cloud densities only exacerbate the situation.

4. THE OVERALL PICTURE OF N49 AND ITS ENVIRONS

We now discuss N49 globally in an attempt to both understand its enormous surface brightness and predict its future evolution. We first summarize the previous discussion. N49 has a filamentary structure in optical maps. Spectral variations between regions of high and low surface brightness are small. Echelle spectra indicate that brightness fluctuations of ≤ 0.8 pc extent exist, which could arise from density variations or projection effects. There is also evidence in the echelle data for faint, fast-moving shocks with velocities 200–270 km s^{-1}. However, these fast shocks cannot contribute appreciably to the emission seen by *IUE* and in the optical (or N v would be much stronger than observed). The optical and X-ray maps indicate a strong interaction with the molecular cloud in the southeast observed by Hughes et al. (1989). From *IUE* spectra, we observe that the bulk of the UV emission appears to be associated with the bright optical filaments. This is consistent with shock models which indicate that the majority of C IV λ1550 emission is emanating from shocks ≤ 140 km s^{-1}. Furthermore, the modeling indicates that a distribution of shock velocities, hence densities, must be present. Densities averaging roughly 150 cm^{-3}, but possibly ranging from 20 to 940 cm^{-3}, are prevalent. Long et al. (1981), by use of the volume emissivity of the X-ray gas, inferred a preshock density of 0.8 cm^{-3} for N49. By using an improved measure of the X-ray diameter (20 pc) from the reprocessed data, as well as an updated value of the emissivity of 4.0×10^{-23} ergs cm^3 s^{-1} (Hamilton, Sarazin, & Chevalier 1983, scaled to LMC abundances), we obtain an average preshock density of 0.90 cm^{-3}. Thus, the basic reason that N49 has such a high surface brightness is that it is encountering dense material, mainly in the form of a CO cloud to the southeast of the remnant.

The filamentary appearance of optical emission, and the spectral uniformity across features varying greatly in brightness, suggest a rippled sheet emission picture as described by Hester (1987). In this model, shocks driven into large clouds (see Hester & Cox 1986) emit in sheets, mimicking the spatial extent of the clouds. Thus filamentary structure occurs as sheets crinkle along the line of sight and are viewed alternately edge-on and face-on. Faint emission occurs where sheets are viewed more face-on, while tangencies to the line of sight result in bright filaments. Intensity ratios of the emission lines do not depend upon geometry, so the ratio maps of Figure 2 are remarkably flat. This picture also provides a natural explanation for the echelle data. The bright bands show intensities corresponding to their depths along the line of sight and velocity widths corresponding to their rippling.

In the Cygnus Loop, the northeast, "carrot," and west optical emission regions each correspond to a large rippled sheet which, if observed from the distance of N49, would appear as long, marginally resolved filaments. Where the echelle slit crossed each of these filaments, we would see a bright band about 100 km s^{-1} wide, with fainter emission extending to higher velocities (see Kirshner & Taylor 1976; Shull & Clarke 1991; Shull & Hippelein 1991). In the Cygnus Loop the width of the bright emission is comparable to the shock velocity, indicating ripples of about 30° to the line of sight. The velocity centroids range from near zero velocity in the northeast to about -100 km s^{-1} in the carrot, values similar to the N49 observations. The diffuse emission seen in the N49 echelle data must include a mixture of more face-on shocks over a range of velocities (see Shull & Clarke 1991).

We now demonstrate the consistency of our view of N49's local ISM and the validity of our previous modeling assumptions. For a radius of R pc and homogeneous intercloud density $n_{\rm ICM}$ cm^{-3}, where the clouds do not inhibit the flow of the main blast wave, the Sedov (1959) solution yields the following relation between blast wave velocity and initial explosion energy $E_{51} = E/(10^{51}$ ergs):

$$V_b = 2.2 \times 10^4 \left(\frac{E_{51}}{n_{\rm ICM}}\right)^{1/2} R^{-3/2} , \qquad (2)$$

where V_b is the blast wave velocity in kilometers per second. An explosion energy of $E_{51} = 1$ yields a present V_b of 730 km s^{-1} and an inferred age of 5.4×10^3 yr for N49. Primarily because of a more accurate measure of the SNR diameter, this age estimate is somewhat lower than the estimate of Long et al. (1981). The postshock temperature as a function of velocity is a straightforward result of the continuity equations across the shock front (cf. McKee & Hollenbach 1980):

$$T = 14KV^2 , \qquad (3)$$

where V is the shock velocity in kilometers per second, and K is an ionization factor, equal to 1 for the case of a fully ionized preshock gas, and 2 for the neutral case.

We may approximate the cooling time for a parcel of gas by taking the enthalpy density and dividing by the volume cooling rate, viz.,

$$t_{\rm cool} = \frac{(5/2)n_{\rm tot}\,kT}{n_{\rm H}\,n_e\,\Lambda(T)} , \qquad (4)$$

where $n_{\rm tot}$ is the total (ion plus electron) density. We take the cooling function $\Lambda(T)$ as $9.0 \times 10^{-20} T^{-1/2}$ ergs cm^3 s^{-1}, from Raymond, Cox, & Smith (1976), adjusted to LMC abundances. Letting $K = 1$, $n = 1.1 n_{\rm H}$, $n_e = 1.1n$, $n_c = 0.25n$ (to account for the factor of 4 density increase upon passage through the shock), and using equation (3), we have, for the cooling time of a shock with velocity V (km s^{-1}) and preshock density n_c (cm^{-3}),

$$t_{\rm cool} = 3.4 \times 10^{-3} \frac{V^3}{n_c} \text{ yr} . \qquad (5)$$

Assuming equilibrium in the pressure driving the main blast wave and cloud shock, we have from McKee & Cowie (1975), $\beta' n_{\rm ICM} V_b^2 = n_c V^2$, for a shock of velocity V driven into the cloud. The factor β' is a measure of the pressure enhancement driving the shock into the cloud. For large clouds $\beta' \sim 3$. We may rewrite equation (5) as

$$t_{\rm cool} = 3.4 \times 10^{-3} \frac{\beta'^{3/2} n_{\rm ICM}^{3/2} V_b^3}{n_c^{5/2}} \text{ yr} . \qquad (6)$$

For a blast wave of 730 km s^{-1} and preshock cloud density of 150 cm^{-3}, the implied cloud shock velocity is 100 km s^{-1}. This agrees well with the densities and velocities required to explain the observed luminosities. From equation (6), we see that clouds with densities ≥ 30 cm^{-3}, corresponding to shock velocities ≤ 230 km s^{-1}, having cooling times ≤ 1200 yr. Thus this model can explain the faint high-velocity emission seen in echelle spectra.

Shull et al. (1985) have proposed a model for the evolution of N49 in which the progenitor star of N49, while on the main sequence, evaporated all clouds (except the densest molecular clouds) within its Strömgren radius. Mass that flowed outside this radius recombined. After the progenitor became a red supergiant, the gas within the Strömgren sphere recombined, and the neutral outer shell expanded inward, creating an exponential radial density distribution within this shell. In this picture, the ISM presently existing around N49 would thus be the direct result of the evolution of postulated initial conditions involving the lasting influence of the progenitor star. In this sense the model is very structured, resulting in a highly ordered ISM including a density-enhanced shell.

Relying on the interaction of the blast wave with a high-density shell, the Shull et al. model seeks to explain the long-slit echelle data of Shull (1983). Our alternative model attributes the interaction of the main blast wave with dense material to the accidental presence of the CO cloud observed at the southeast edge of N49 by Hughes et al. (1989). The character of the long-slit echelle data is a natural consequence of the rippled sheet geometry. Shull (1983) appeals to moving clouds to explain the echelle data bands. This leads to an expectation of photoionization precursor "spikes" at the cloud velocities, but none are seen. Shull et al. (1985) suggest that ~200–270 km s^{-1} shocks emitting faintly in [O III] (Shull 1983) are a manifestation of the main blast wave running up the exponential radial density gradient shell ($n_0 \sim 100$ cm^{-3}). However, our modeling indicates that, for the same preshock density, shocks moving at 200–270 km s^{-1} will emit about 3 times as much emission in [O III] as a shock at 120 km s^{-1}. Thus the shell, as opposed to interior clouds, should be visible as a separate entity, but it is not observed in our [O III] image. A similar argument applies to C IV λ1550, but, to the contrary, *IUE* position B shows that C IV appears to be associated only with the bright interior shocks and not with the main blast wave. Finally, the preshock densities of 20–940 cm^{-3} that we report are also incompatible with the Shull et al. model.

5. CONCLUSIONS

Through a comparison of LMC abundance shock wave models and optical and *IUE* UV spctra of N49, we find that a range of shock velocities must be spatially widespread. Most of the emission seen optically and by *IUE* emanates from shocks with velocities ≤140 km s^{-1}. The *IUE* UV emission appears to be closely associated with the optical emission; there does not appear to be detectable UV emission in the *IUE* range from the main blast wave (i.e., ahead of the bright optical emission). We have fitted a power law of shock velocities from 40 to 270 km s^{-1} to the optical/UV observations. The agreement is encouraging and provides a connection between shocks of very fast and slow velocities.

High densities are the major reason for N49's striking brightness in both the X-ray and optical regions of the spectrum. The radiative emission arises in clouds with preshock density between 20 and 940 cm^{-3}, whereas X-ray data indicate an average intercloud medium density of 0.90 cm^{-3}. The cloud densities that we report are much larger than had been previously estimated from [S II] λλ6717, 6731.

We report estimates of the total intrinsic luminosity of N49 in several optical and UV lines. We have constructed optical line ratio maps and have shown that, in particular, a bright ridge of enhanced emission in the [O III]:[O I] and [O III]:Hα maps arises from photoionization precursors, in harmony with Shull's (1983) interpretation of the narrow [O III] spike seen in echelle observations. Nonradiative shock emission from fast shocks encountering partly neutral material may be present around the periphery of the remnant, but the presence of both shock precursors and nearby H II regions makes nonradiative Balmer emission less likely to exist and more difficult to detect.

We have developed an alternative view that to of Shull et al. (1985) of the ISM local to N49. The data suggests that the prevailing ISM is unaffected by the progenitor star. We have analyzed whether a Sedov solution and clouds several parsecs in extent can be responsible for the bulk of the optical and UV emission. Sheets of emission where the blast wave encounters a molecular cloud can naturally explain the bright optical filaments, the lack of spectral variation with brightness, and the long-slit echelle data. The energetics of the remnant's evolution as a whole and blast wave/cloud interactions on a smaller scale appear to be self-consistent and suggest a main blast wave velocity of 730 km s^{-1} and a present age of 5.4×10^3 yr for N49. Densities are high enough for shocks ≥200 km s^{-1} to become radiative, as required by the echelle spectra.

Variations in reddening are apparent across the face of N49 on spatial scales as small as 2″, with an average $E(B-V) \simeq 0.37$. Particular lines of sight show $E(B-V)$ as high as 0.9, while others appear to have no extinction whatsoever. We have for the first time in a SNR detected a new emission feature in the *IUE* LWP spectrum at 2628 Å. Although no candidates for this line are especially pleasing, we suggest that [Ti III] may be responsible and propose a test of this hypothesis. We have also for the first time measured the temperature in the C^0 zone of the recombination flow behind a SNR shock wave, finding $T \simeq 8.5 \times 10^3$ K.

We are pleased to acknowledge the staffs of the Las Campanas and *International Ultraviolet Explorer* Observatories for their help in procuring the optical and UV data, as well as F. Seward for providing us with the reprocessed *Einstein* X-ray data. We also thank Skip Westphal for expert assistance with Figures 1 and 2. We are grateful for support from the Center for Astrophysical Sciences. This project is in partial fulfillment of O. V.'s Ph.D dissertation at The Johns Hopkins University. This research was partially supported by NASA *IUE* grant NAG 5-988 to The Johns Hopkins University.

APPENDIX

DISCUSSION OF POSSIBLE IDENTIFICATIONS FOR λ2628

Since N49 shows many faint lines of Fe in both the optical and the IR, one might suspect that the feature at 2628 Å is due to an ion of Fe. A survey of the energy levels of Fe from Fuhr, Martin, & Wiese (1988) shows that no energy levels in any of the ions exist such that a forbidden transition to a ground-state configuration would result in a line at ~2628 Å. The only permitted ground-state–connected iron ion transition leading to a line at this wavelength is Fe II $a\,^6D$–$z\,^6D^o$. However, using the values of A and f from Fuhr et al. (1988), we find for thermal equilibrium of the ground-state multiplet that the ratio of lines ~2600 Å ($j = 9/2 \rightarrow 9/2$,

$5/2 \rightarrow 7/2$) to lines ~ 2628 Å ($j = 9/2 \rightarrow 7/2$, $7/2 \rightarrow 5/2$, $5/2 \rightarrow 3/2$, $3/2 \rightarrow 1/2$) is 2:1. Assuming the nonequilibrium case, where only the lowest level ($j = 9/2$) is occupied in the ground state before collisional excitation, raises this ratio to 4.4:1. This is clearly incompatible with the observations. Moreover, a heretofore unknown fluorescence mechanism must be discarded as well, since *each* individual upper level preferentially branches to lines other than 2628 Å.

[Mg VII] at 2629 Å is another possible identification. This is a carbon-like ion, the transition corresponding to $2p^2\,{}^1D \rightarrow 2p^2\,{}^3P_2$. Although we are not aware of any published transition rates from this upper level, scanning Mendoza (1983) indicates that carbonic ions emit ${}^1D \rightarrow {}^3P_2$ and ${}^1D \rightarrow {}^3P_1$ in an expected ratio of $\sim 3:1$. Another line at 2509 Å is thus expected at about $\frac{1}{3}$ the strength of the 2629 Å feature, should it be due to [Mg VII]. The observations do not support this.

Still another possibility is Cr III $4p\,{}^3H \rightarrow 4s\,{}^3H$, $4p\,{}^1H \rightarrow 4s\,{}^1H$. We have identified [Cr II] lines in the IR spectra reported above, so a higher ionization Cr line in the UV must not be eliminated out of hand. However, each of these Cr III transitions has accompanying expected lines which are not seen. Furthermore, none of these transitions are ground-state–connected, making collisional excitation very unlikely. For Cr the same upper-level electron configuration gives rise to a 2628 Å line in either the singlet or the triplet case. However, unless some fluorescence mechanism creates a high population of this upper state, the high (~ 15 eV) excitation potential is difficult to overcome for the electron gas $\leq 10^5$ K, since electrons energetic enough to excite this level from the ground state fall in the exponential tail of the Maxwellian distribution.

Forbidden [Ti III] surprisingly seems to be the most likely possibility we have identified. The transition under consideration is $3d4s\,{}^3D \rightarrow 3d^2\,{}^3F$, where both upper and lower levels are even. The lower level is the ground state, while the upper level is metastable. Although the collision strengths for this transition are not known, the upper-state multiplet splitting yields three strong lines between 2626 and 2630 Å, which, due to the *A* coefficients found in Martin et al. (1988), will be the strongest lines regardless of the upper-level population distribution. The possible 2607 Å feature cannot be explained via [Ti III], and also the relative abundance of Ti is very low, leading to concern. Thus, with reservations, we believe [Ti III] to be responsible for the 2628 Å feature. In the main body of the paper we suggest an observational test of this hypothesis.

REFERENCES

Badnell, N. R. 1991, ApJ, 379, 356
Benvenuti, P., D'Odorico, S., & Dopita, M. 1979, Nature, 277, 99
Benvenuti, P., Dopita, M., & D'Odorico, S. 1980, ApJ, 238, 601
Blair, W. P., & Kirshner, R. P. 1985, ApJ, 289, 582
Blair, W. P., Kirshner, R. P., & Chevalier, R. A. 1981, ApJ, 247, 879
———. 1982, ApJ, 254, 50
Blair, W. P., et al. 1991a, ApJ, 379, L33
Blair, W. P., Long, K. S., Vancura, O., & Holberg, J. B. 1991b, ApJ, 374, 202
Bohlin, R. C. 1986, ApJ, 301, 1001
Chevalier, R. A., Kirshner, R. P., & Raymond, J. C. 1980, ApJ, 235, 186
Christensen, R. B., & Watson, W. D. 1981, Phys. Rev. A, 24, 1331
Chu, Y.-H., & Kennicutt, R. C. 1988, AJ, 95, 1111
Clark, D. H., Tuohy, I. R., Long, K. S., Szymkowiak, A. E., Dopita, M. A., Mathewson, D. S., & Culhane, J. L. 1982, ApJ, 255, 440
Cline, T. L., et al. 1982, ApJ, 255, L45
Cox, D. P. 1972, ApJ, 178, 143
Cox, D. P., & Raymond, J. C. 1985, ApJ, 298, 651
Danziger, I. J., & Leibowitz, E. M. 1985, MNRAS, 216, 365
Dennefeld, M. 1986, A&A, 157, 267
Dopita, M. A. 1979, ApJS, 40, 455
Dopita, M. A., Binette, L., D'Odorico, S., & Benvenuti, P. 1984, ApJ, 276, 653
Dopita, M. A., Binette, L., & Schwartz, R. D. 1982, ApJ, 261, 183
Drake, G. W. F. 1971, Phys. Rev. A, 3, 908
Dufour, R. J. 1984, in IAU Symp. 108, Structure and Evolution of the Magellanic Clouds, ed. S. van den Bergh & K. S. de Boer (Dordrecht: Reidel), 353
Dupree, A. K., Kirshner, R. P., Nassiopoulos, G. E., Raymond, J. C., & Sonneborn, G. 1987, ApJ, 320, 597
Eastman, R. G., & Kirshner, R. P. 1989, ApJ, 347, 771
Eissner, W., & Zeippen, C. J. 1981, J. Phys. B, 14, 2125
Fitzpatrick, E. L. 1985, ApJ, 299, 219
Fuhr, J. R., Martin, G. A., & Wiese, W. L. 1988, J. Phys. Chem. Ref. Data, Vol. 17, Suppl. 4
Giovanardi, C., Natta, A., & Palla, F. 1987, A&AS, 70, 269
Graham, J. R., Evans, A., Albinson, J. S., Bode, M. F., & Meikle, W. P. S. 1987, ApJ, 319, 126
Gunn, J. E., & Westphal, J. A. 1981, Proc. SPIE, 290, 16
Hamilton, A. J. S., Sarazin, C. L., & Chevalier, R. A. 1983, ApJS, 51, 115
Hester, J. J. 1987, ApJ, 314, 187
Hester, J. J., & Cox, D. P. 1986, ApJ, 300, 675
Howarth, I. D. 1983, MNRAS, 203, 301
Hughes, J. P., Bronfman, L., & Nyman, L. 1989, Supernovae, ed. S. E. Woosley (New York: Springer-Verlag), 679
Hummer, D. G., & Storey, P. J. 1987, MNRAS, 224, 801
Kirshner, R. P., & Taylor, K. 1976, ApJ, 208, L83
Long, K. S., Helfand, D. J., & Grabelsky, D. A. 1981, ApJ, 248, 925
Martin, G. A., Fuhr, J. R., & Wiese, W. L. 1988, J. Phys. Chem. Ref. Data, Vol. 17, Suppl. 3
Mathewson, D. S., Ford, V. L., Dopita, M. A., Tuohy, I. R., Long, K. S., & Helfand, D. J. 1983, ApJS, 51, 345
Mathewson, D. S., Ford, V. L., Tuohy, I. R., Mills, B. Y., & Turtle, A. J. 1985, ApJS, 58, 197
Mathewson, D. S., Healey, J. R., & Westerlund, B. E. 1963, Nature, 199, 681
McKee, C. F., & Cowie, L. L. 1975, ApJ, 195, 715
McKee, C. F., & Hollenbach, D. J. 1980, ARA&A, 18, 219
Mendoza, C. 1983, in IAU Symp. 103, Planetary Nebulae, ed. D. R. Fowler (Dordrecht: Reidel), 143
Osterbrock, D. E. 1989, Astrophysics of Gaseous Nebulae and Active Galactic Nuclei (Mill Valley: University Science Books)
Osterbrock, D. E., & Dufour, R. J. 1973, ApJ, 185, 441
Raymond, J. C. 1979, ApJS, 39, 1
Raymond, J. C., Black, J. H., Dupree, A. K., Hartmann, L., & Wolff, R. S. 1980, ApJ, 238, 881
Raymond, J. C., Cox, D. P., & Smith, B. W. 1976, ApJ, 204, 290
Raymond, J. C., Hester, J. J., Cox, D., Blair, W. P., Fesen, R. A., & Gull, T. R. 1988, ApJ, 324, 869
Russell, S. C., & Dopita, M. A. 1990, ApJS, 74, 93
Savage, B. D., & de Boer, K. S. 1981, ApJ, 243, 460
Savage, B. D., & Mathis, J. S. 1979, ARA&A, 17, 73
Seaton, M. J. 1979, MNRAS, 187, 73P
Sedov, L. I. 1959, Similarity and Dimensional Methods in Mechanics (New York: Academic)
Shull, J. M., & McKee, C. F. 1979, ApJ, 227, 131
Shull, P. 1983, ApJ, 275, 611
Shull, P., & Clarke, M. W. 1991, PASP, 103, 811
Shull, P., Dyson, J. E., Kahn, F. D., & West, K. A. 1985, MNRAS, 212, 799
Shull, P., & Hippelein, H. 1991, ApJ, 383, 714
Smith, R. C., Kirshner, R. P., Blair, W. P., & Winkler, P. F. 1991, ApJ, 375, 652
Stone, R. P. S., & Baldwin, J. A. 1983, MNRAS, 204, 347
Tucker, W. H., & Koren, M. 1971, ApJ, 168, 283
Whitford, A. E. 1958, AJ, 63, 201